TOPICAL REVIEW — Magnetism, magnetic materials, and interdisciplinary research

Crystal structures, phase relationships, and magnetic phase transitions of R_5M_4 compounds (R = rare earths, M = Si, Ge)*

Ouyang Zhong-Wen(欧阳钟文)[a] and Rao Guang-Hui(饶光辉)[b]†

[a] Wuhan National High Magnetic Field Center, Huazhong University of Science and Technology, Wuhan 430074, China
[b] School of Materials Science and Engineering, Guilin University of Electronic Technology, Guilin 541004, China

(Received 17 June 2013)

Our recent studies of the crystal structures, phase transitions, and magnetic properties of intermetallic compounds R_5M_4 (R = rare earths; M = Si, Ge) are reviewed briefly. First, crystal structures, phase relationships, and magnetic properties of several 5:4 compounds, including $Nd_5Si_{4-x}Ge_x$, $Pr_5Si_{4-x}Ge_x$, $Gd_{5-x}La_xGe_4$, La_5Si_4, and Gd_5Sn_4, are presented. In particular, the canted spin structures as well as the magnetic phase transitions in $Pr_5Si_2Ge_2$ and Pr_5Ge_4 investigated by neutron powder diffractions and small-angle neutron scattering are reviewed. Second, the crystal structures and magnetic properties of the most studied compounds $Gd_5(Si,Ge)_4$ are summarized. The focus is on the parent compound Gd_5Ge_4, which is an amazing material exhibiting magnetic anisotropy, angular dependent spin-flop transition, metastable magnetic response, Griffiths-like phase, thermal effect under pulsed fields, antiferromagnetic and ferromagnetic resonances, pronounced effects of impurities, and high-field induced magnetic transitions.

Keywords: crystal structure, phase relationship, magnetic phase transition

PACS: 75.30.Kz, 75.30.Sg, 61.66.Dk **DOI:** 10.1088/1674-1056/22/9/097501

1. Introduction

The magnetocaloric effect (MCE), often referred to as an adiabatic temperature change (ΔT_{ad}) or an isothermal magnetic entropy change (ΔS_M) driven by an applied magnetic field, is a phenomenon common to all magnetic materials due to the coupling of the magnetic sublattice with the magnetic field. Magnetic refrigeration based on MCE is a revolutionary, highly energy efficient, and environmentally friendly cooling technology.[1–5] One of the most important ingredients for the commercialization of this state-of-the-art technique is the availability of new magnetic materials that exhibit giant MCE near room temperature. In 1997, Pecharsky *et al.*[6,7] at Ames Laboratory, USA reported that the pseudobinary alloys $Gd_5(Si_xGe_{1-x})_4$ manifest large MCE. The Curie temperature and MCE of these materials can be tuned and optimized by varying the Si/Ge ratio. As a result, the compound with $x = 0.5$, i.e., $Gd_5Si_2Ge_2$, exhibits an extremely large ΔT_{ad} or ΔS_M (hereafter denoted as giant MCE) near 290 K, which is 10 times larger than that of the pure Gd metal, the best known room-temperature magnetic refrigerant material at that time.[8,9] This milestone discovery took magnetic refrigeration much closer to large-scale commercial application, simulating wide enthusiasm in searching for room-temperature magnetocaloric materials. Up to date, a wealth of materials exhibiting large or unusual MCE have been successively found, for instance, RM_2 (R = rare earths; M = Al, Co, Ni),[10–13] $Mn(As_{1-x}Sb_x)$,[14–16] $MnFe(P_{1-x}As_x)$,[17–19] $La(Fe_{1-x}Si_x)_{13}$,[20–22] and manganites $R_{1-x}M_xMnO_3$ (M = Ca, Sr, Ba).[23–25] The giant MCE in materials is usually concomitant with a first-order magnetostructural phase transition, i.e., simultaneous magnetic and crystallographic transformations.

In the family of R_5M_4 (M = carbon group elements), the most studied materials are $Gd_5(Si_xGe_{1-x})_4$ due to their giant MCE.[6,7,26–30] Figure 1 shows the temperature–composition (T–x) phase diagram of this system.[31] The compounds with $x >\sim 0.58$ have an orthorhombic (O(I)) structure at high temperature. Upon cooling they undergo a second-order ferromagnetic (FM) ordering transition without a change of the crystal structure. The Curie temperature T_C decreases with decreasing x. For $x \leq\sim 0.5$, $Gd_5(Si_xGe_{1-x})_4$ compounds undergo a first-order FM ordering phase transition that is always coupled with a crystallographic transformation. This region is divided into two different composition ranges. For $0.4 \leq x \leq 0.5$, a first-order magnetostructural transition occurs between high-temperature monoclinic (M) paramagnetic (PM) phase and low-temperature Gd_5Si_4-type O(I) FM phase. Since the T_C is near room temperature, the MCE has been intensively investigated within this composition range. A first-order magnetostructural transition takes place between Sm_5Ge_4-type O(II) PM phase and O(I) FM phase for $0.24 < x < 0.3$, and a first-order magnetostructural transition occurs between

*Project supported by the National Natural Science Foundation of China (Grants Nos. 50025102 and 50631040), the National Basic Research Program of China (Grant No. 2006CB601101), the Exchange Program between NIST and the Chinese Academy of Sciences, and the Natural Science Foundation of Guangxi Province, China (Grant No. 2012GXNSFGA060002).

†Corresponding author. E-mail: rgh@guet.edu.cn

© 2013 Chinese Physical Society and IOP Publishing Ltd

O(II) antiferromagnetic (AFM) phase and O(I) FM phase for $x < 0.24$, following a second order O(II) PM to O(II) AFM transformation. Figure 2 shows the crystal structures of O(II) and O(I) phases in the case of Gd_5Ge_4,[32] where the Ge–Ge bonds between slabs are broken and connected, respectively. The M phase for $0.4 \leq x \leq 0.5$ is a monoclinic distortion of the O(II) phase with half of the Si/Ge-Si/Ge bonds connected between slabs, which is not shown here. Besides the giant MCE, $Gd_5(Si_xGe_{1-x})_4$ compounds present several other interesting phenomena: giant magnetoresistance,[33–35] colossal magnetostriction,[36–38] spontaneous generation of voltage,[39,40] unusual training effect,[41] dynamical and thermal phenomena,[42,43] acoustic emissions,[44] and a novel glass-like kinetically retarded state.[45,46] It is believed that all these properties are closely associated with the magnetostructural transition.

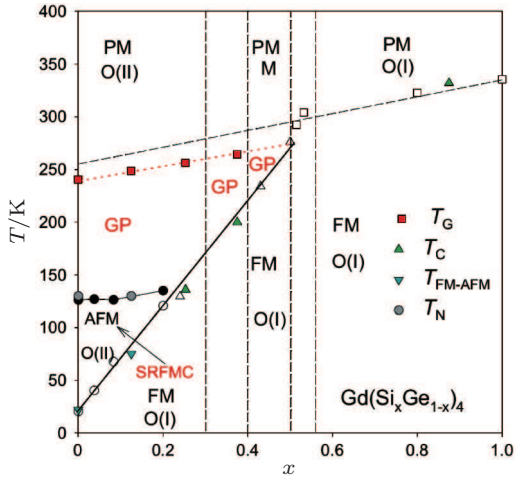


Fig. 1. Low field T–x phase diagram of $Gd_5(Si_{1-x}Ge_x)_4$. The PM regime below the T_G line is the GP-like regime. The short range FM correlation in the AFM regime is denoted as SRFMC.[31]

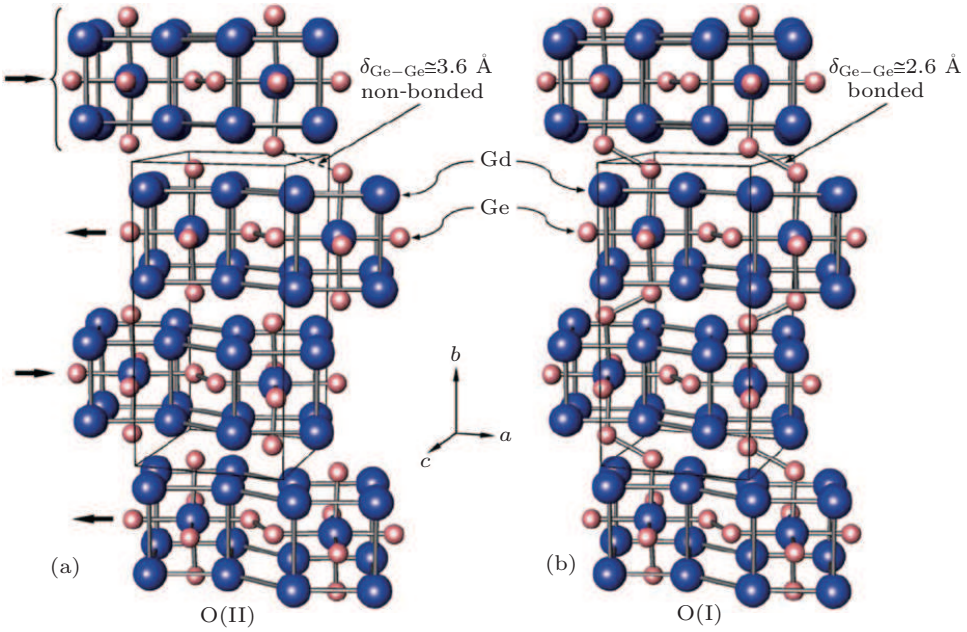


Fig. 2. Perspective views of the crystal structures of Gd_5Ge_4 (a) in the PM and AFM states and (b) in the FM state. The bracket on the top left in panel (a) highlights a single slab. The numerical values indicate the interslab Ge–Ge distances in both structures. The arrows in panel (a) illustrate directions in which the slabs shear during the O(II) to O(I) transformation.[32]

The second most studied R:Si(Ge) 5:4 system is $Tb_5(Si_xGe_{1-x})_4$,[47–52] which has crystal structure and phase relationships (T–x diagram) identical to those of $Gd_5(Si_xGe_{1-x})_4$. The almost collinear magnetic structure[53,54] is also similar to the Gd alloys. The differences lie in the composition ranges for different phases[49] and the anisotropic critical fields for triggering the PM–FM transition in the Tb compounds.[55] In the Tb alloys, the composition range for O(II) and M phases shrinks to small x values. In the aspect of magnetism, the Tb alloys present a spin reorientation transition and a strong magnetic anisotropy due to the strong single-ion anisotropy of the 4f wave function, which are not observed or absent in the Gd compounds due to the spherical 4f wave function ($J = S = 7/2$, $L = 0$). Interestingly, in the $Tb_5Si_2Ge_2$ compound, the magnetic and structural transitions are decoupled, that is, there is a temperature difference of about 8 K between the magnetic and the structural transitions.[53] Under a certain pressure, the two transitions are again coupled.[56]

A similar decoupling of the magnetic and structural transitions is found in Er_5Si_4,[57–60] in which the first-order structural transition from high-temperature O(I) structure to the low-temperature M structure occurs within 160–220 K, while the FM ordering takes place below $T_C = 30$ K, with a temperature separation much larger than that in $Tb_5Si_2Ge_2$. The magnetic properties of Er_5Si_4 are very complicated, depend-

ing on the magnetic field, temperature, and pressure.[61–63] Er_5Si_4 is found to undergo a field-induced crystallographic transition, but without a magnetic transition. This is a rare phenomenon and is the first example for the R_5M_4 materials. High magnetic field-induced volume magnetostriction supports the field-induced structural transition.[61] Crystal structures and magnetic properties of other 5:4 materials, for instance, $R_5(Si_xGe_{1-x})_4$ (R = La, Ce, Pr, Nd, Dy, Ho), $Gd_5(Si_xSn_{1-x})_4$, and so on, were also intensively investigated and the details about them can be found in other review articles and references therein.[2,5]

In this article, we review our research results on some R_5M_4 compounds in the past decade. In Section 2, we focus on the crystal structures, phase relationships, and magnetic properties of several 5:4 materials, including $Nd_5Si_{4-x}Ge_x$, $Pr_5Si_{4-x}Ge_x$, $Gd_{5-x}La_xGe_4$, La_5Si_4, and Gd_5Sn_4, studied by X-ray powder diffractions (XRD), neutron powder diffractions (NPD), and magnetization measurements with superconducting quantum interference device (SQUID) magnetometer. In Section 3, we summarize several interesting magnetic properties of the most studied system $Gd_5(Si,Ge)_4$, in particular, Gd_5Ge_4. These properties were studied by magnetization measurements using the SQUID magnetometer, pulsed high magnetic fields, and high-field electron spin resonance (ESR).

2. Crystal structures, phase relationships, and magnetic properties of some R_5M_4 alloys

Early in the 1960s, Smith *et al.* discovered the R_5Si_4 and R_5Ge_4 phases.[64–66] At room temperature, the compounds R_5Si_4 with R = La, Ce, Pr, and Nd crystallize in the tetragonal Zr_5Si_4-type structure and those with R = Sm, Gd, Tb, Dy, Er, and Y in the orthorhombic Gd_5Si_4-type structure, while all R_5Ge_4 alloys crystallize in the orthorhombic Sm_5Ge_4-type structure. The crystallographic structures of some R_5Ge_4 alloys with R = heavy rare earths were further confirmed by Holtzberg *et al.*[67] Although these alloys were reported almost 40 years ago, detailed structural data are still lacking. The knowledge of magnetic and crystallographic structures of these alloys is indispensable for understanding the microscopic physical mechanisms controlling the observed intriguing properties. In the following, we outline the results of our studies on the crystal structures and phase relationships of some 5:4 alloys, together with their magnetic properties.

2.1. $Nd_5Si_{4-x}Ge_x$

2.1.1. Crystal structure and phase relationship of $Nd_5Si_{4-x}Ge_x$

Room temperature XRD patterns of $Nd_5Si_{4-x}Ge_x$ show that the Nd_5Si_4-based alloys crystallize in the tetragonal Zr_5Si_4-type structure with space group $P4_12_12$ and the Nd_5Ge_4-based alloys crystallize in the orthorhombic Gd_5Ge_4-type structure (O(II)) with space group *Pnma*. There are two ternary intermediate phases crystallizing in the orthorhombic Gd_5Si_4-type structure (O(I)) with space group *Pnma* and the monoclinic $Gd_5Si_2Ge_2$-type structure with space group $P112_1/a$, respectively.[68,69] The Rietveld refinement technique has been used to refine the crystal structure. Figure 3 shows the experimental and calculated XRD patterns as well as their differences for four representative compounds at room temperature, Nd_5Si_4, $Nd_5Si_{2.8}Ge_{2.2}$, $Nd_5Si_2Ge_2$, and Nd_5Ge_4. The atomic and lattice parameters of the compounds are listed in Tables 1 and 2, respectively. The latter three compounds are structurally correlated and basically can be viewed as layered structures with atom layers stacking along the b direction.

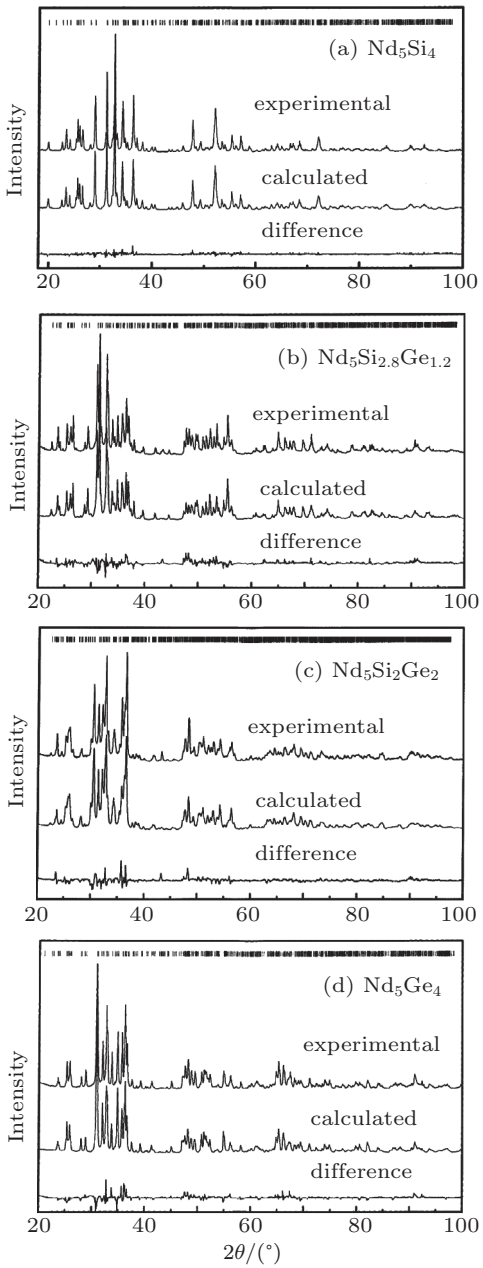


Fig. 3. Experimental and calculated XRD patterns of (a) Nd_5Si_4, (b) $Nd_5Si_{2.8}Ge_{1.2}$, (c) $Nd_5Si_2Ge_2$, and (d) Nd_5Ge_4, and the differences between them. The vertical bars indicate the expected Bragg reflection positions.[69]

Table 1. Atomic parameters of Nd_5Si_4, $Nd_5Si_{2.8}Ge_{1.2}$, $Nd_5Si_2Ge_2$, and Nd_5Ge_4.

Atom	x/a	y/b	z/c
Nd_5Si_4[68]			
Nd1 (4*a*)	0.3129(3)	0.3129(3)	0.0000(0)
Nd2 (8*b*)	0.3696(3)	0.0114(3)	0.4542(1)
Nd3 (8*b*)	0.1300(3)	–0.0155(2)	0.8742(2)
Si1 (8*b*)	0.1871(14)	0.1638(12)	0.6945(6)
Si2 (8*b*)	0.2864(15)	0.9349(13)	0.0627(7)
$Nd_5Si_{2.8}Ge_{1.2}$			
Nd1 (4*c*)	0.3520(8)	0.2500(0)	0.01687(7)
Nd2 (8*d*)	0.0290(5)	0.0987(2)	0.1808(5)
Nd3 (8*d*)	0.3135(5)	0.8782(2)	0.1819(5)
*M*1[a] (4*c*)	0.2288(16)	0.2500(0)	0.3610(15)
*M*2 (4*c*)	0.9986(12)	0.2500(0)	0.9128(28)
*M*3 (8*d*)	0.1486(21)	0.9479(7)	0.4846(16)
$Nd_5Si_2Ge_2$			
Nd1 (4*e*)	0.3377(12)	0.2476(4)	0.0041(8)
Nd2a (4*e*)	–0.0040(7)	0.1001(4)	0.1799(9)
Nd2b (4*e*)	0.0196(8)	0.3976(4)	0.1818(9)
Nd3a (4*e*)	0.3669(9)	0.8834(4)	0.1665(9)
Nd3b (4*e*)	0.3256(9)	0.6223(4)	0.1787(9)
*M*1[a] (4*e*)	0.1988(20)	0.2500(10)	0.3696(16)
*M*2 (4*e*)	0.9471(26)	0.2563(13)	0.8991(26)
*M*3a (4*e*)	0.2059(21)	0.9616(10)	0.4771(18)
*M*3b (4*e*)	0.1460(22)	0.5587(10)	0.4680(18)
Nd_5Ge_4			
Nd1 (4*c*)	0.2913(7)	0.2500(0)	0.0035(6)
Nd2 (8*d*)	–0.0214(4)	0.1011(2)	0.1804(4)
Nd3 (8*d*)	0.3817(4)	0.8854(2)	0.1614(4)
Ge1 (4*c*)	0.1744(10)	0.2500(0)	0.3618(12)
Ge2 (4*c*)	0.9088(12)	0.2500(0)	0.8924(11)
Ge3 (8*d*)	0.2221(9)	0.9529(4)	0.4733(9)

[a] *M* = (Si, Ge)

Figure 4 shows the composition dependences of the lattice parameters and unit cell volume of $Nd_5Si_{4-x}Ge_x$ at room temperature. Four structurally distinct phase regions are well defined. For the Nd_5Si_4-based solid solution (phase T), the lattice parameter *a* increases gradually with increasing *x*, while the parameter *c* varies slightly. In the narrow region of the Gd_5Si_4-type O(I) phase, both *a* and *c* increase gradually with increasing Ge content, but *b* seems to decrease. For the $Gd_5Si_2Ge_2$-type M phase and the Nd_5Ge_4-based solid solution (O(II) phase), *a*, *b*, and *c* all increase with *x*. Between these well defined phase regions are three two-phase regions. The unit cell volume of the alloy increases with increasing substitution of Ge for Si, which is consistent with the relative sizes of the Si and Ge atoms.

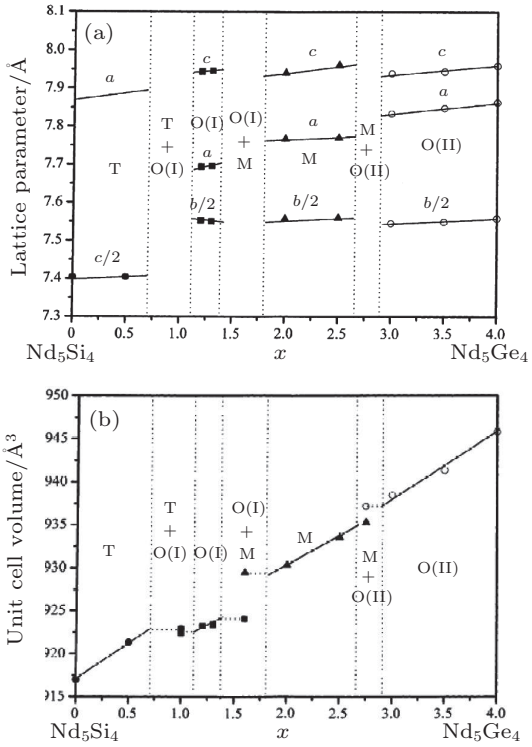


Fig. 4. The *x* dependencies of (a) lattice parameters and (b) unit cell volume for $Nd_5Si_{4-x}Ge_x$ at room temperature. The dashed lines show the phase regions, where T and O(II) are the tetragonal-based and orthorhombic-based solid solutions, respectively, and O(I) and M are the ternary orthorhombic and monoclinic intermediate phases.[69]

Table 2. Crystal structure data of $Nd_5Si_{4-x}Ge_x$.

Composition *x*	Space group	*a*/Å	*b*/Å	*c*/Å	γ/(°)	V/Å^3
0	$P4_12_12$	7.8694(0)	7.8694(0)	14.8077(1)	90	917.00
0.5	$P4_12_12$	7.8878(1)	7.8878(1)	14.8084(4)	90	921.34
1.0	$P4_12_12$	7.9035(3)	7.9035(3)	14.7753(4)	90	922.95
	Pnma	7.6907(3)	15.1044(5)	7.9380(3)	90	922.40
1.2	*Pnma*	7.6939(1)	15.1054(3)	7.9439(1)	90	923.24
1.3	*Pnma*	7.6954(4)	15.1013(8)	7.9461(4)	90	923.42
1.6	*Pnma*	7.6967(4)	15.1055(16)	7.9483(5)	90	924.09
	$P112_1/a$	7.7712(4)	15.1129(8)	7.9293(5)	93.57(0)	929.46
2.0	$P112_1/a$	7.7674(2)	15.1133(2)	7.9409(2)	93.60(0)	930.34
2.5	$P112_1/a$	7.7704(3)	15.1189(7)	7.9614(4)	93.50(0)	933.57
2.75	$P112_1/a$	7.7817(3)	15.1192(6)	7.9508(4)	93.48(0)	933.72
	Pnma	7.8246(4)	15.0966(8)	7.9337(6)	90	937.16
3.0	*Pnma*	7.8335(3)	15.0906(11)	7.9389(4)	90	938.48
3.5	*Pnma*	7.8484(2)	15.0983(6)	7.9441(2)	90	941.36
4.0	*Pnma*	7.8631(1)	15.1163(3)	7.9559(1)	90	945.65

The high-temperature crystallographic phases were obtained by annealing the as-arc-melted alloys at 1273 K for one week, followed by water quenching.[70] The lattice parameters are listed in Table 3. Figure 5 shows the composition dependences of the lattice parameters and unit cell volume of the alloys. Three structurally distinct phase regions are determined: the Nd_5Si_4-type solid solution with the tetragonal Zr_5Si_4-type structure (space group $P4_12_12$), the Nd_5Ge_4-based solid solution with the Gd_5Ge_4-type O(II) structure (space group *Pnma*), and a ternary intermediate phase with the monoclinic $Gd_5Si_2Ge_2$-type structure (space group $P112_1/a$). As compared with the room-temperature phase relationship, the intermediate O(I) phase disappears and the composition range for the tetragonal phase is much extended. It is worth noting that in contrast to the case of $Gd_5(Si_xGe_{1-x})_4$, the room-temperature and the high-temperature phases of $Nd_5Si_{2.8}Ge_{1.2}$ and $Nd_5Si_2Ge_2$ are not structurally correlated.

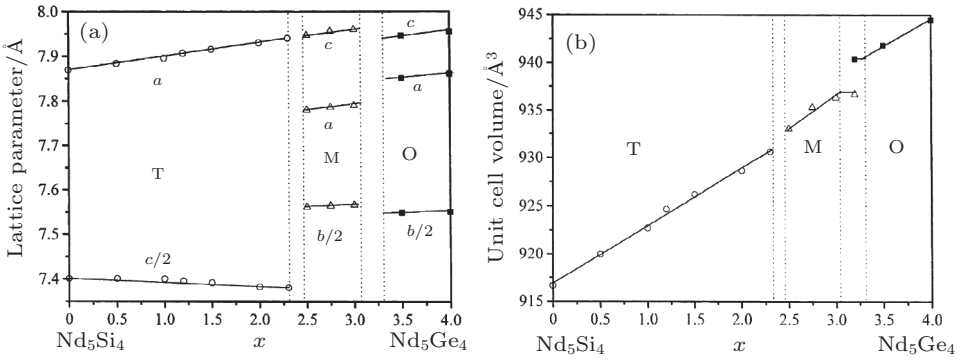


Fig. 5. The x dependencies of (a) lattice parameters and (b) unit cell volume for $Nd_5Si_{4-x}Ge_x$ at 1273 K. The dashed lines show the phase regions, where T and O are the tetragonal-based and orthorhombic-based solid solutions, respectively, and M is the ternary monoclinic intermediate phase.[70]

Table 3. Crystal structure data of $Nd_5Si_{4-x}Ge_x$ at 1273 K. The space group given in parentheses is the one at ambient temperature.[69]

Composition x	Space group	a/Å	b/Å	c/Å	γ/(°)	V/Å^3
0	$P4_12_12$ ($P4_12_12$)	7.8695(1)	7.8695(1)	14.8018(3)	90	916.66
0.5	$P4_12_12$ ($P4_12_12$)	7.8837(1)	7.8837(1)	14.8017(3)	90	919.97
1.0	$P4_12_12$[b)]	7.8957(1)	7.8957(1)	14.8010(3)	90	922.73
1.2	$P4_12_12$ (*Pnma*)	7.9068(0)	7.9068(0)	14.7907(1)	90	924.69
1.5	$P4_12_12$[c)]	7.9153(1)	7.9153(1)	14.7837(3)	90	926.23
2.0	$P4_12_12$ ($P112_1/a$)	7.9304(1)	7.9304(1)	14.7661(1)	90	928.66
2.3	$P4_12_12$ ($P112_1/a$)	7.9399(1)	7.9399(1)	14.7624(3)	90	930.65
2.5	$P112_1/a$ ($P112_1/a$)	7.7805(3)	15.1232(7)	7.9464(5)	93.69(0)	933.08
2.75	$P112_1/a$[d)]	7.7860(4)	15.1295(8)	7.9558(6)	93.59(0)	935.35
3.0	$P112_1/a$(Pnma)	7.7907(4)	15.1322(8)	7.9594(7)	93.69(0)	936.38
3.2[a)]	$P112_1/a$[a)]	7.7921(7)	15.1335(14)	7.9602(11)	93.71(0)	936.71
	Pnma[a)]	7.8493(5)	15.0842(15)	7.9427(6)	90	940.43
3.5	*Pnma* (*Pnma*)	7.8512(2)	15.0983(7)	7.9457(2)	90	941.88
4.0	*Pnma* (*Pnma*)	7.8617(2)	15.1027(7)	7.9548(2)	90	944.50

[a)] Located in the *Pnma* phase region at ambient temperature. [b)] Located in the $P4_12_12 + Pnma$ two–phase region at ambient temperature.

[c)] Located in the $Pnma + P112_1/a$ two–phase region at ambient temperature. [d)] Located in the $P112_1/a + Pnma$ two–phase region at ambient temperature.

2.1.2. Magnetic properties of $Nd_5Si_{2.8}Ge_{1.2}$ and $Nd_5Si_2Ge_2$

The magnetic properties of the compounds $Nd_5Si_{2.8}Ge_{1.2}$ and $Nd_5Si_2Ge_2$ were studied for both the room-temperature phase (α-phase) and the high-temperature (1273 K) phase (β-phase).[71] Figure 6 shows the zero-field-cooled (zfc) and field-cooled (fc) heating $M(T)$ curves of these compounds. The irreversibility between the zfc and fc curves is the characteristic of spin glass-like behavior. The Curie temperature T_C of α-$Nd_5Si_{2.8}Ge_{1.2}$ is higher than that of β-$Nd_5Si_{2.8}Ge_{1.2}$. In contrast, the T_C of α-$Nd_5Si_2Ge_2$ is lower than that of β-$Nd_5Si_2Ge_2$. (The anomaly at ~93 K is due to a minority phase.) Interestingly, the T_C of β-$Nd_5Si_{2.8}Ge_{1.2}$ and that of β-$Nd_5Si_2Ge_2$ are almost the same despite an appreciable difference in the Ge content. These differences in T_C can be understood within the Ruderman–Kittel–Kasuya–Yosida (RKKY) approximation. According to Callaway,[72] the effective exchange interaction is of relatively long range, decreasing as

r^{-3} (r is the interatomic distance of magnetic atoms). Thus, as r decreases, T_C of the compound increases. In addition, according to Bleaney-Bleaney,[73] within the molecule field approximation the magnetic ordering temperature increases with increasing conduction electron concentration. These two models imply that a compound with shorter r and higher conduction electron concentration, which can be determined by the Zintl–Klemn formalism,[74] will have a higher magnetic ordering temperature. Among the four compounds, the average interatomic distance r_{av} between Nd atoms in α-$Nd_5Si_{2.8}Ge_{1.2}$ is the shortest, but the conduction electron concentration is the highest, giving rise to the highest T_C. The β-$Nd_5Si_{2.8}Ge_{1.2}$ and β-$Nd_5Si_2Ge_2$ have the same conduction electron concentration and a similar r_{av} value, which accounts for their similar T_C.

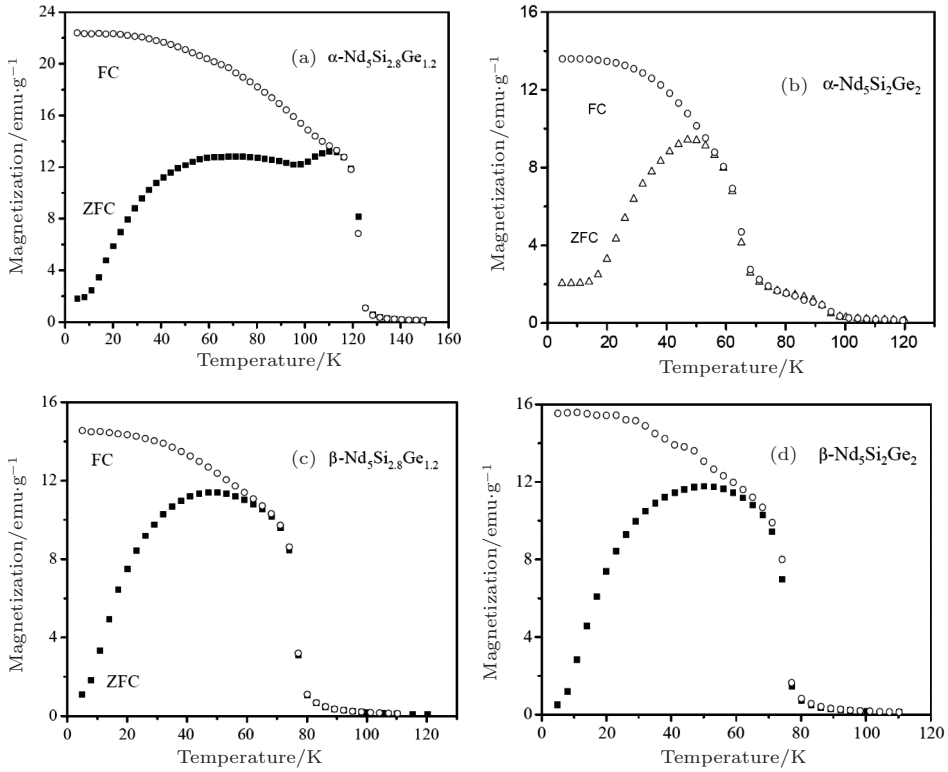


Fig. 6. The zfc heating and fc cooling $M(T)$ curves at 0.05 T for α phase ((a) and (b)) and β phase ((c) and (d)) of $Nd_5Si_{2.8}Ge_{1.2}$ and $Nd_5Si_2Ge_2$.[71]

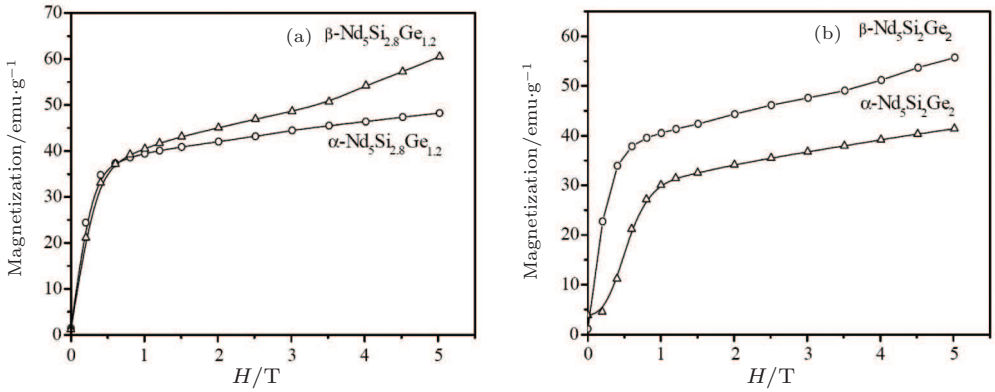


Fig. 7. The $M(H)$ curves at 5 K for α- and β-phases of (a) $Nd_5Si_{2.8}Ge_{1.2}$ and (b) $Nd_5Si_2Ge_2$.[71]

Figure 7 shows the $M(H)$ curves at 5 K of these compounds. It reveals that the α phase is more difficult to magnetize and has lower magnetization than the β phase. The magnetic moment at 5 T varies from 1.3 μ_B/Nd to 1.89 μ_B/Nd, much lower than the saturated value of a free Nd^{3+} ion ($gJ = 3.27\ \mu_B$), which is probably due to the canted magnetic structure. Both the canted magnetic structure and the spin glass-like state of these compounds may arise from a competition

between nearest-neighbor Nd–Nd FM and Nd–Nd AFM interactions.

2.2. $Pr_5Si_{4-x}Ge_x$

2.2.1. Crystal structure and phase relationship of $Pr_5Si_{4-x}Ge_x$

The room temperature XRD patterns of $Pr_5Si_{4-x}Ge_x$ show that the Pr_5Si_4-based alloys crystallize in the tetragonal Zr_5Si_4-type structure with space group $P4_12_12$ and the Pr_5Ge_4-based alloys crystallize in the orthorhombic Sm_5Ge_4-type structure with space group *Pnma*. In contrast to the $Nd_5Si_{4-x}Ge_x$ system, there is only one ternary intermediate phase crystallizing in the monoclinic $Gd_5Si_2Ge_2$-type structure with space group $P112_1/a$.[75] Figure 8 shows the Rietveld refinement results of three representative compounds, Pr_5Si_4, $Pr_5Si_2Ge_2$, and Pr_5Ge_4. Their atomic and lattice parameters are listed in Tables 4 and 5, respectively.

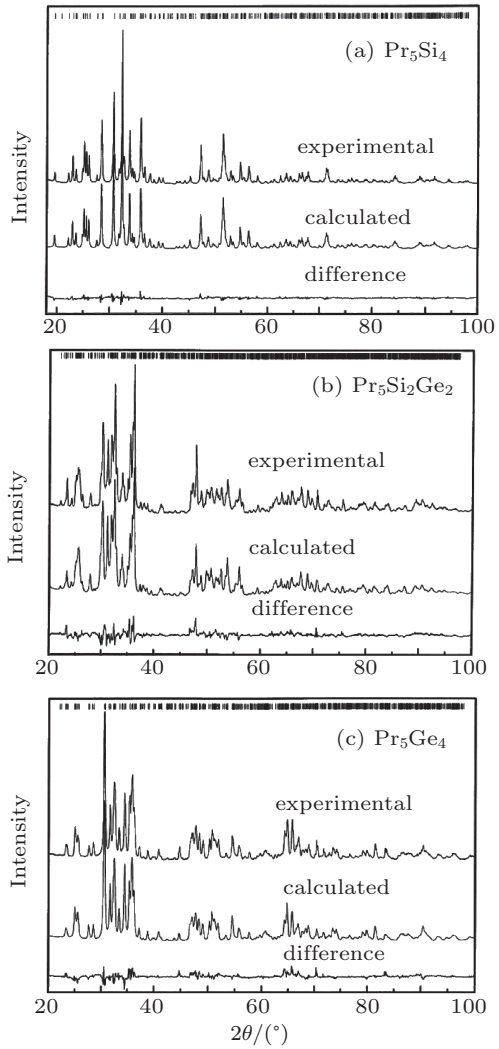


Fig. 8. Experimental and calculated XRD patterns of (a) Pr_5Si_4,(b) $Pr_5Si_2Ge_2$, and (c) Pr_5Ge_4, and the differences between them. The vertical bars indicate the expected Bragg reflection positions.[75]

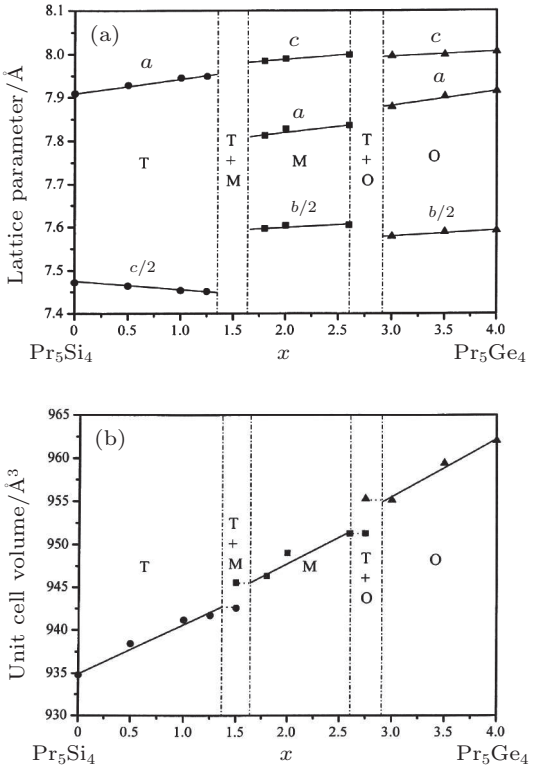


Fig. 9. The x dependencies of (a) lattice parameters and (b) unit cell volume for $Pr_5Si_{4-x}Ge_x$ at room temperature. The dashed lines show the phase regions, where T and O are the tetragonal-based and orthorhombic-based solid solutions, respectively, and M is the ternary monoclinic intermediate phase.[75]

Table 4. Atomic parameters of Pr_5Si_4, $Pr_5Si_2Ge_2$, and Pr_5Ge_4.

Atom	x/a	y/b	z/c
Pr_5Si_4			
Pr1 (4*a*)	0.3116(3)	0.3116(3)	0.0000(0)
Pr2 (8*b*)	0.3700(3)	0.0125(3)	0.4531(1)
Pr3 (8*b*)	0.1292(3)	–0.0149(2)	0.8747(2)
Si1 (8*b*)	0.1863(14)	0.1658(12)	0.6964(6)
Si2 (8*b*)	0.2869(14)	0.9279(13)	0.0588(7)
$Pr_5Si_2Ge_2$			
Pr1 (4*e*)	0.3419(10)	0.2482(4)	0.0000(7)
Pr2a (4*e*)	–0.0054(7)	0.1000(3)	0.1831(8)
Pr2b (4*e*)	0.0233(7)	0.3965(3)	0.1802(8)
Pr3a (4*e*)	0.3638(8)	0.8840(3)	0.1633(8)
Pr3b (4*e*)	0.3271(8)	0.6230(3)	0.1769(7)
*M*1[a] (4*e*)	0.1993(16)	0.2465(8)	0.3770(14)
*M*2 (4*e*)	0.9475(21)	0.2602(11)	0.8954(21)
*M*3a (4*e*)	0.2159(21)	0.9560(10)	0.4654(18)
*M*3b (4*e*)	0.1526(21)	0.5552(9)	0.4672(19)
Pr_5Ge_4			
Pr1 (4*c*)	0.2859(6)	0.2500(0)	–0.0010(6)
Pr2 (8*d*)	–0.0222(3)	0.1019(2)	0.1809(4)
Pr3 (8*d*)	0.3818(3)	0.8863(2)	0.1615(4)
Ge1 (4*c*)	0.1707(9)	0.2500(0)	0.3682(11)
Ge2 (4*c*)	0.9121(10)	0.2500(0)	0.8939(10)
Ge3 (8*d*)	0.2207(7)	0.9523(3)	0.4727(8)

[a] M = 0.5Si + 0.5Ge.

Figure 9 shows the composition dependences of the lattice parameters and unit cell volume of $Pr_5Si_{4-x}Ge_x$ at room temperature. Three structurally distinct phase regions are well defined. In the Pr_5Si_4-based solid solution (phase T), the lattice parameter a increases with increasing x, while the c decreases. In the $Gd_5Si_2Ge_2$-type M phase and the Pr_5Ge_4-based solid solution (phase O(II)), a, b, and c all increase with increasing x. Between these well defined phase regions are two two-phase regions. The phase relationship is basically similar to that of the Nd-based compounds (Subsection 2.1.1), except for the missing of an intermediate O(I) phase and the difference in phase boundaries. The unit cell volume of the alloy increases with increasing substitution of Ge for Si, also similar to the case of the Nd-based compounds (Subsection 2.1.1).

Table 5. Crystal structure data of $Pr_5Si_{4-x}Ge_x$.

Composition x	Space group	a/Å	b/Å	c/Å	γ/(°)	V/Å^3
0	$P4_12_12$	7.9092(0)	7.9092(0)	14.9437(1)	90	934.80
0.5	$P4_12_12$	7.9286(1)	7.9286(1)	14.9285(3)	90	938.44
1.0	$P4_12_12$	7.9459(1)	7.9459(1)	14.9068(3)	90	941.17
1.25	$P4_12_12$	7.9492(1)	7.9492(1)	14.9030(3)	90	941.72
1.5	$P4_12_12$	7.9576(1)	7.9576(1)	14.8847(4)	90	942.55
	$P112_1/a$	7.8103(4)	15.2077(8)	7.9735(6)	93.77(0)	945.54
1.8	$P112_1/a$	7.8127(2)	15.1930(7)	7.9849(5)	93.70(0)	946.33
2.0	$P112_1/a$	7.8282(1)	15.2072(3)	7.9902(2)	93.82(0)	949.07
2.6	$P112_1/a$	7.8360(3)	15.2089(5)	7.9991(4)	93.75(0)	951.27
2.75	$P112_1/a$	7.8388(7)	15.2042(14)	7.9971(11)	93.58(0)	951.29
	Pnma	7.8730(5)	15.1801(15)	7.9881(6)	90	955.26
3.0	*Pnma*	7.8786(4)	15.1569(13)	7.9966(5)	90	955.11
3.5	*Pnma*	7.9022(2)	15.1774(8)	7.9992(3)	90	959.38
4.0	*Pnma*	7.9141(1)	15.1829(3)	8.0060(1)	90	961.99

Table 6. Crystal structure data of $Pr_5Si_{4-x}Ge_x$ at 1273 K. The space group given in parentheses is the one at ambient temperature.[75]

Composition x	Space group	a/Å	b/Å	c/Å	V/Å^3
0	$P4_12_12$ ($P4_12_12$)	7.9098(1)	7.9098(1)	14.9462(2)	935.11
1.0	$P4_12_12$ ($P4_12_12$)	7.9401(1)	7.9401(1)	14.9100(3)	940.00
1.5	$P112_1/a$[a)]	7.9552(1)	7.9552(1)	14.9029(3)	943.12
2.0	$P4_12_12$ ($P112_1/a$)	7.9725(1)	7.9725(1)	14.8855(1)	946.13
2.5	$P4_12_12$ ($P112_1/a$)	7.9892(1)	7.9892(1)	14.8683(3)	949.00
2.8	$P4_12_12$[b)]	8.0011(1)	8.0011(1)	14.8510(3)	950.73
3.0	*Pnma* (*Pnma*)	7.8858(3)	15.1661(10)	7.9842(3)	954.90
3.5	*Pnma* (*Pnma*)	7.8999(2)	15.1725(7)	7.9924(2)	957.98
4.0	*Pnma* (*Pnma*)	7.9147(2)	15.1869(7)	8.0069(2)	962.43

[a)] Located in the $Pnma + P112_1/a$ two–phase region at ambient temperature.

[b)] Located in the $P112_1/a + Pnma$ two–phase region at ambient temperature.

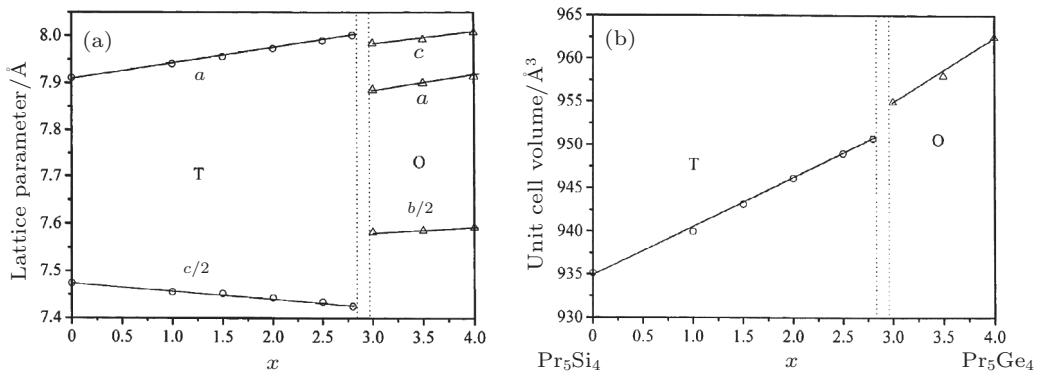


Fig. 10. The x dependencies of (a) lattice parameters and (b) unit cell volume for $Pr_5Si_{4-x}Ge_x$ at 1273 K. The dashed lines show the phase regions, where T and O are the tetragonal-based and orthorhombic-based solid solutions, respectively.[70]

The phase relationships of $Pr_5Si_{4-x}Ge_x$ at high-temperature (1273 K) were also investigated.[70] The lattice parameters are listed in Table 6. Figure 10 shows the composition dependences of the lattice parameters and unit cell volume of the alloys. Two structurally distinct phase regions are defined: the Pr_5Si_4-type solid solution with the tetragonal Zr_5Si_4-type structure (space group $P4_12_12$) and the Pr_5Ge_4-based solid solution with the Gd_5Ge_4-type structure (O(II) type, space group *Pnma*). As compared to the room-temperature phase relationship, the intermediate M phase disappears and the composition range for the tetragonal phase is much extended. It is worth noting that for $Pr_5Si_2Ge_2$, the room-temperature and the high-temperature phases are not structurally correlated, in contrast to the case of $Gd_5(Si_xGe_{1-x})_4$.

2.2.2. Magnetic properties of $Pr_5Si_{4-x}Ge_x$

Figure 11 shows the zfc and fc heating $M(T)$ curves of three representative compounds, Pr_5Si_4, $Pr_5Si_2Ge_2$, and Pr_5Ge_4, located in three different phase regions at room temperature.[76,79] Like the Nd-based compounds (Subsection 2.1.2), all of the $M(T)$ curves show an fc/zfc irreversibility, which may originate from the spin glass-like state. For $Pr_5Si_2Ge_2$, the small anomaly around 60 K could be attributable to the contribution of a minor tetragonal impurity phase. For Pr_5Ge_4, two magnetic transitions are observed under a low field. The low-temperature anomaly may be associated with a transition between two different spin structures. Interestingly, under a high field of 5 T the low-temperature anomaly disappears, which implies the occurrence of a field-driven metamagnetic transition. The Ge content dependence of T_C is illustrated in Fig. 12, where the ordering temperatures (T_C and Néel temperature T_N) of $R_5Si_{4-x}Ge_x$ (R = Dy, Tb, Gd)[49,77] are also plotted for comparison. For heavy rare earths, the orthorhombic Gd_5Si_4-type O(I) structure has the highest magnetic ordering temperature, whereas the orthorhombic Sm_5Ge_4-type O(II) structure has the lowest one, which can be well understood according to Kirchmayr *et al.*[78] within the RKKY approximation including the conduction electron concentration. However, this is not the situation for the light rare earth element Pr, suggesting that the T_C is not exclusively contributed by the conduction electron concentration. According to Callaway's model,[72] the average interatomic distance r_{av} between the magnetic Pr atoms in the M symmetry is the largest among all the phases, which leads to the lowest T_C of these compounds. Note that this model is invalid for explaining the composition dependence of T_C in the T and O(II) phases.

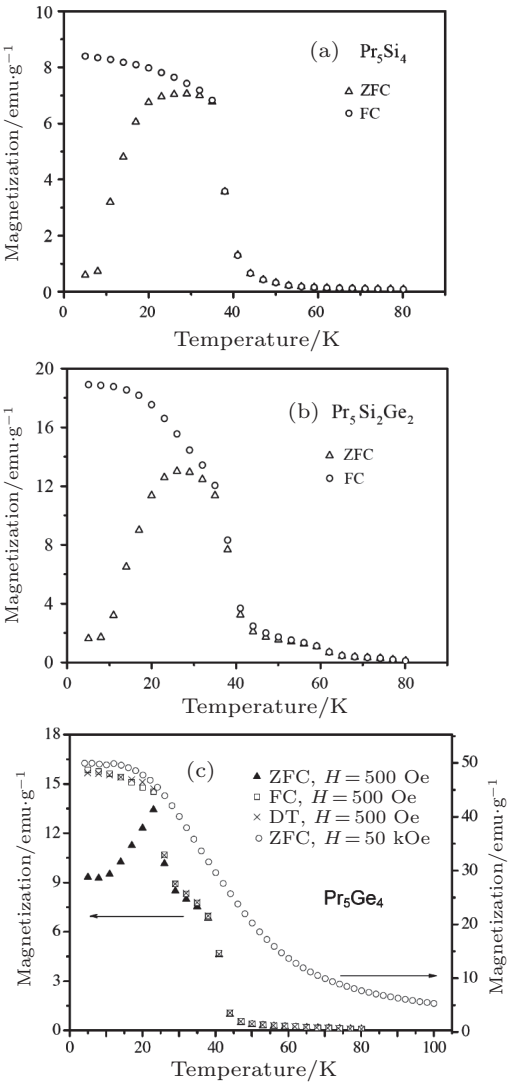


Fig. 11. The zfc heating and fc cooling $M(T)$ curves for (a) Pr_5Si_4, (b) $Pr_5Si_2Ge_2$ ($H = 0.05$ T), and (c) Pr_5Ge_4 ($H = 0.05$ T and 5 T). DT shows a measurement of cooling.[76,79]

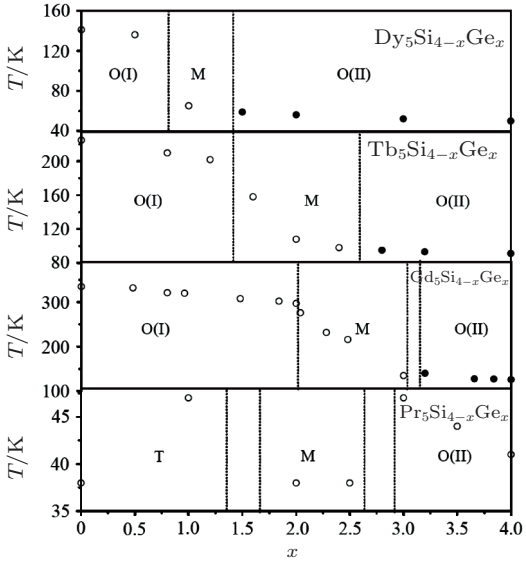


Fig. 12. The T_C vs x relationship of $Pr_5Si_{4-x}Ge_x$. The ordering temperatures of $R_5Si_{4-x}Ge_x$ (R = Dy, Tb, Gd)[49,77] are also plotted for comparison. The open and the filled circles represent T_C and T_N, respectively. The dashed lines delineate phase regions, where T, O(I), and O(II) are the tetragonal Zr_5Si_4-type, orthorhombic Gd_5Si_4-type, and Sm_5Ge_4-type solid solutions, respectively, and M is the ternary monoclinic intermediate phase.[76]

Figure 13(a) shows the $M(H)$ curves measured at 5 K for Pr_5Si_4, $Pr_5Si_2Ge_2$, and Pr_5Ge_4. The magnetic moment at 5 T varying from 1.61 μ_B/Pr to 1.82 μ_B/Pr is much lower than the saturated value of a free Pr^{3+} ion ($gJ = 3.20$ μ_B), which is probably caused by the magnetocrystalline anisotropy of the Pr ions and the canted magnetic structure. The latter may arise from a competition between nearest-neighbor Pr–Pr FM and AFM interactions. For Pr_5Ge_4, a metamagnetic-like anomaly is observed at ~ 2 T, which can be attributed to a transition between two different magnetic structures. Figure 13(b) shows that the high-temperature $M(H)$ curves have a typical FM-like behavior.[79] The metamagnetic-like feature observed at 5 K is hardly observed at high temperature. The temperature dependence of the electrical resistivity of Pr_5Ge_4, which is not shown here but can be found in Ref. [79], also exhibits two kinks due to magnetic transitions, consistent with the $M(T)$ measurement.

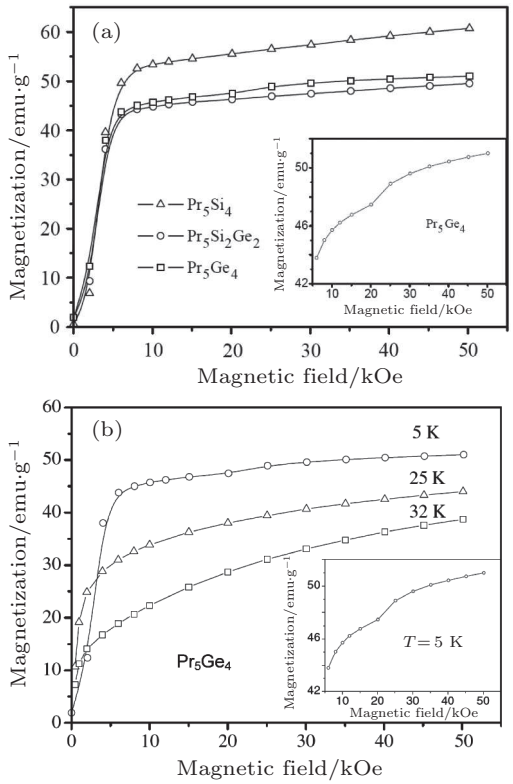


Fig. 13. The $M(H)$ curves (a) at 5 K for $Pr_5Si_{4-x}Ge_x$ and (b) at 5–32 K for Pr_5Ge_4. The inset shows a possible metamagnetic transition near 2 T for Pr_5Ge_4.[76,79]

The $M(T)$ and $M(H)$ curves of high-temperature (1273 K) phase β-$Pr_5Si_2Ge_2$ are shown in Figs. 14 and 15, respectively, in which the room-temperature phase data are also plotted for comparison.[80] The main features are (i) T_C of the β-$Pr_5Si_2Ge_2$ phase is higher than that of the room-temperature phase α-$Pr_5Si_2Ge_2$, quite similar to the case of $Nd_5Si_2Ge_2$ (see Fig. 6); (ii) the $M(H)$ curve is S-shaped and may be attributed to a metamagnetic transition or a characteristic of the spin glass-like state, also similar to the case of $Nd_5Si_2Ge_2$ (see Fig. 7); (iii) the β-$Pr_5Si_2Ge_2$ phase is more difficult to magnetize and has lower magnetization than α-$Pr_5Si_2Ge_2$, in contrast to $Nd_5Si_2Ge_2$ (see Fig. 7).

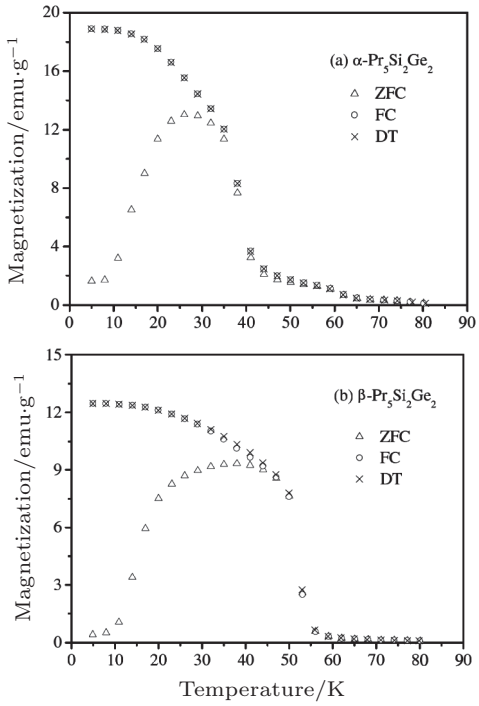


Fig. 14. The zfc and fc $M(T)$ curves at 0.05 T for (a) α-phase and (b) β-phase $Pr_5Si_2Ge_2$. DT stands for the decreasing temperature measurement.[80]

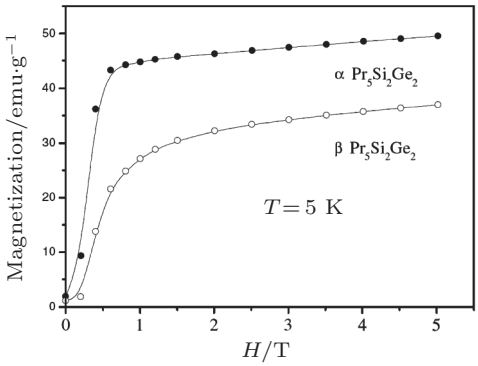


Fig. 15. The $M(H)$ curves at 5 K for α- phase and β-phase $Pr_5Si_2Ge_2$.[80]

2.2.3. Magnetic and crystal structures of $Pr_5Si_2Ge_2$ and Pr_5Ge_4

As illustrated above, the results of magnetization measurements, e.g., the much lower magnetic moment than that of free Pr^{3+} and the two magnetic transitions in Pr_5Ge_4, imply the presence of complicated (canted or noncollinear) spin structures in $Pr_5Si_{4-x}Ge_x$. To explore the magnetic and crystal structures, temperature-dependent neutron powder diffraction (NPD) and small-angle neutron scattering (SANS) experiments have been carried out on $Pr_5Si_2Ge_2$[81] and Pr_5Ge_4.[82]

The NPD patterns of $Pr_5Si_2Ge_2$ show that the high-temperature tetragonal $Pr_5Si_2Ge_2$ crystallizes in the Zr_5Si_4-type structure with the space group $P4_12_12$ down to 4 K. Figure 16 displays the experimental and calculated NPD patterns at 300 K and 4 K. The temperature dependencies of the integrated intensity of the (001) peak and the peak intensity of the (110) reflection are shown in Fig. 17. Obviously, a long-range magnetic ordering takes place at T_C= 52 K, in agreement with the magnetization measurement (see Fig. 14). The magnetic structure can be modeled with the magnetic space group $P4_12_1'2'$. The magnetic structure derived from the Rietveld refinement (see Table 7 and Fig. 18) shows a net FM component exclusively along the c axis. No other magnetic transition is manifested below T_C. The lattice parameters shown in Fig. 19 vary continuously around T_C with a small negative magneto-volume effect, indicating a second-order phase transition. Refinements of temperature-dependent NPD data reveal that the magnetic ordering of the Pr atoms develops simultaneously on different sites.

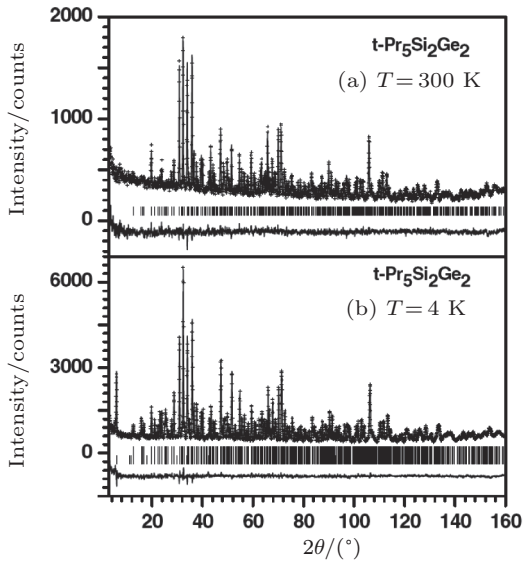


Fig. 16. Experimental (cross) and calculated (solid line) NPD patterns for tetragonal $Pr_5Si_2Ge_2$ at (a) 300 K and (b) 4 K. Differences between the experimental and calculated patterns are shown at the bottom of the figure. The vertical bars indicate the expected nuclear reflection positions. The expected magnetic reflection positions are marked by the bars on the lower row in panle (b).[81]

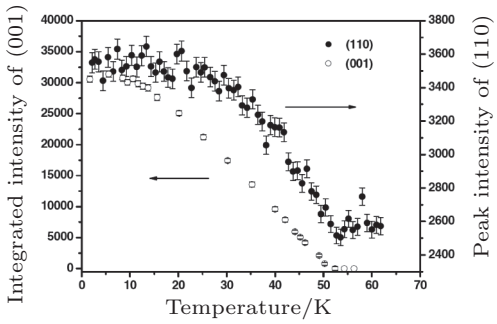


Fig. 17. Temperature dependence of the integrated intensity of (001) peaks and the peak intensity of (110) reflection of tetragonal $Pr_5Si_2Ge_2$ upon warming.[81]

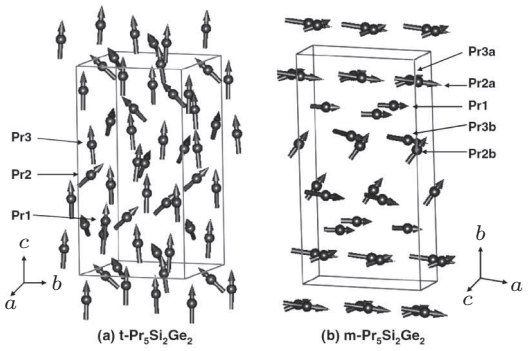


Fig. 18. Magnetic structures of (a) tetragonal $Pr_5Si_2Ge_2$ and (b) monoclinic $Pr_5Si_2Ge_2$. Only the magnetic atoms are shown.[81]

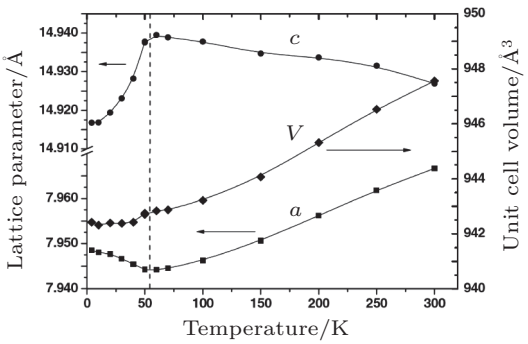


Fig. 19. Temperature dependences of lattice parameters of tetragonal $Pr_5Si_2Ge_2$. The dashed line indicates the position of T_C.[81]

Table 7. Magnetic moment components of Pr atoms in tetragonal-$Pr_5Si_2Ge_2$ at 4 K and 40 K derived from the fitting to NPD data. Magnetic space group is $P4_12_1'2'$.

	μ_x/μ_B	μ_y/μ_B	μ_z/μ_B	μ /μ_B
		T=4 K		
Pr1	–0.29(3)	0.29(3)	2.75(4)	2.78(4)
Pr2	0.18(5)	–1.86(3)	1.69(3)	2.52(3)
Pr3	0.23(5)	0.01(3)	2.81(3)	2.82(3)
		T=40 K		
Pr1	–0.20(12)	0.20(12)	2.46(12)	2.47(12)
Pr2	0.19(16)	–1.09(10)	1.10(8)	1.56(10)
Pr3	–0.04(20)	–0.03(10)	2.24(7)	2.24(7)

NPD patterns were also collected for the monoclinic $Pr_5Si_2Ge_2$, which crystallizes in the $Gd_5Si_2Ge_2$-type structure with the space group $P112_1/a$ down to 4 K. A long-range magnetic ordering occurs at $T_C = 40$ K and the magnetic structure can be modeled with the magnetic space group $P112_1'/a'$. The net magnetic moment lies on the ab plane with the main component along the a axis. No other magnetic transition is observed below T_C. Figures 20 and 21 show the temperature dependences of the peak intensity of the (101) reflection and the experimental and calculated NPD patterns, respectively. The magnetic structure is depicted in Fig. 18, showing the magnetic atoms only. The magnetic moment components of the Pr atoms at 4 K and 30 K are listed in Table 8. The temperature dependence of the lattice parameters is shown in Fig. 22.

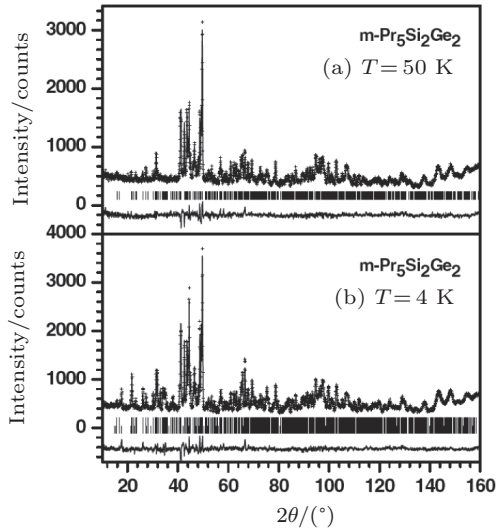


Fig. 20. Experimental (cross) and calculated (solid line) NPD patterns for monoclinic $Pr_5Si_2Ge_2$ at (a) 50 K and 4 K. Differences between the experimental and calculated patterns are shown at the bottom of the figure. The vertical bars indicate the expected nuclear reflection positions. The expected magnetic reflection positions are marked by the bars on the lower row in panel (b).[81]

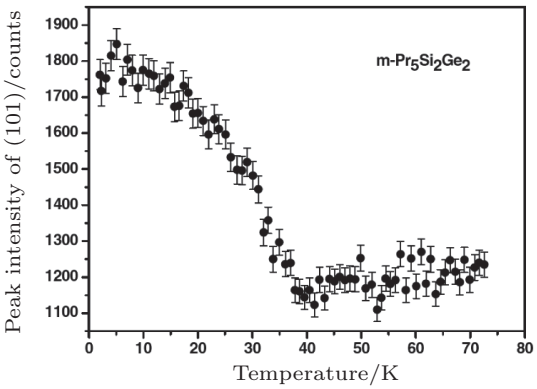


Fig. 21. Temperature dependence of the peak intensity of (101) reflection for monoclinic $Pr_5Si_2Ge_2$ on warming.[81]

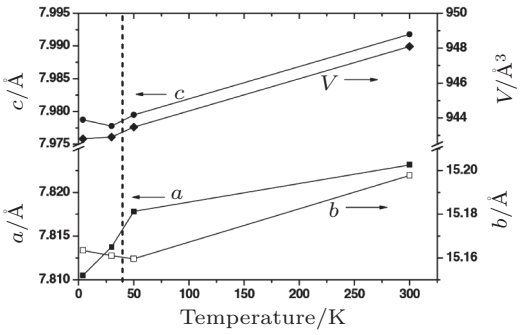


Fig. 22. Temperature dependences of lattice parameters of monoclinic $Pr_5Si_2Ge_2$. The dashed line indicates the position of T_C.[81]

It is now clear that although the tetragonal and the monoclinic phases of $Pr_5Si_2Ge_2$ are not structurally correlated, they exhibit some similarities, e.g., a broad distribution of atomic distance between Pr atoms, similar coordination polyhedrons for Pr atoms, and the same basic building unit [PrM_6]Pr$_8$ (M = Ge or a mixture of Si/Ge), etc.[81] For both phases, the largest change in lattice constant always occurs along the easy magnetization direction of the compound. According to the RKKY interaction model, the competing AFM and FM interactions and the different magnetocrystalline anisotropy on different Pr sites should be responsible for the occurrence of the complex noncollinear magnetic structures of the polymorphic $Pr_5Si_2Ge_2$.

Table 8. Magnetic moment components of Pr atoms in monoclinic-$Pr_5Si_2Ge_2$ at 4 K and 30 K derived from the fitting to NPD data. Magnetic space group is $P112'_1/a'$.

	μ_x/μ_B	μ_y/μ_B	μ_z/μ_B	μ/μ_B
		T=4 K		
Pr1	2.24(5)	0.05(9)	–0.29(8)	2.26(5)
Pr2a	3.03(8)	–0.29(9)	0.27(8)	3.07(9)
Pr2b	1.28(7)	1.94(9)	0.19(8)	2.26(9)
Pr3a	1.92(6)	0.76(9)	0.34(9)	2.04(6)
Pr3b	2.50(7)	–0.52(9)	1.38(9)	2.93(7)
		T = 30 K		
Pr1	1.80(7)	–0.04(15)	–0.25(11)	1.82(7)
Pr2a	2.25(10)	–0.27(14)	–0.04(11)	2.28(11)
Pr2b	0.86(9)	1.12(16)	–0.04(10)	1.36(15)
Pr3a	1.24(7)	0.46(15)	0.52(13)	1.39(9)
Pr3b	1.71(9)	0.07(16)	0.84(15)	1.90(10)

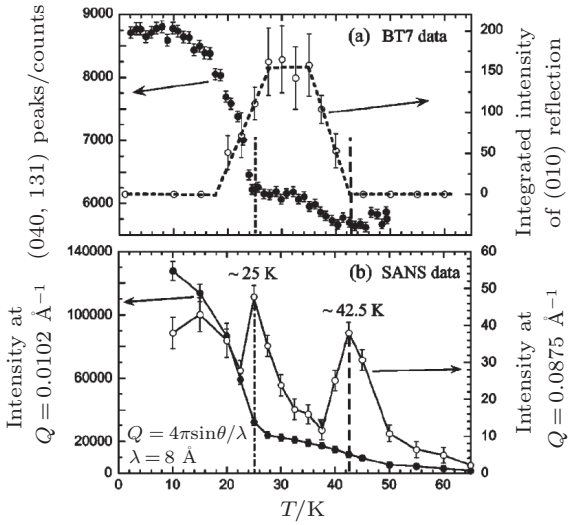


Fig. 23. (a) (131) and (040) magnetic Bragg peaks' intensities (solid circles) and the (010) integrated intensity (open circles). (b) SANS data at $Q = 0.0102$ Å^{-1} (solid circles) and $Q = 0.0875$ Å^{-1} (open circles) as a function of temperature.[82]

The magnetic structure and magnetic phase transitions of Pr_5Ge_4 have been investigated by means of NPD and SANS.[82] Figure 23 shows that both NPD and SANS data indicate the existence of two magnetic phase transitions at 25 K and 42 K, in agreement with the magnetization data (see Fig. 11). A refinement of the crystal structure model based on the high-resolution NPD data showes that from room temperature to 1.6 K, the compound maintains the Sm_5Ge_4-type structure (*Pnma*), in which the Ge atoms occupy two 4*c* sites and one 8*d* site while the Pr atoms occupy two 8*d* sites and one 4*c* site. The refinement of the magnetic structures reveals

that the two magnetic transitions essentially correspond to the long-range orderings of the Pr moments on different crystallographic sites. The Pr moments on the 4*c* site order ferromagnetically with *Pn′ma′* symmetry at 42 K and induce small ordered Pr moments on the 8*d* sites. The long-range ordering of the Pr moments on the 8*d* sites develops at 25 K with *Pnm′a′* symmetry. The separate orderings of the Pr moments on different crystallographic sites can be understood by the salient difference in the rare earth metal environments between the different crystallographic sites. The details on the crystallographic data and magnetic moments of Pr atoms can be found in Table 9 and Ref. [82]. Figure 24 shows the refined magnetic structures for Pr_5Ge_4 at 30 K and 9 K. Thus it is confirmed that the magnetic phase transition around 25 K is a transition between two different spin structures.

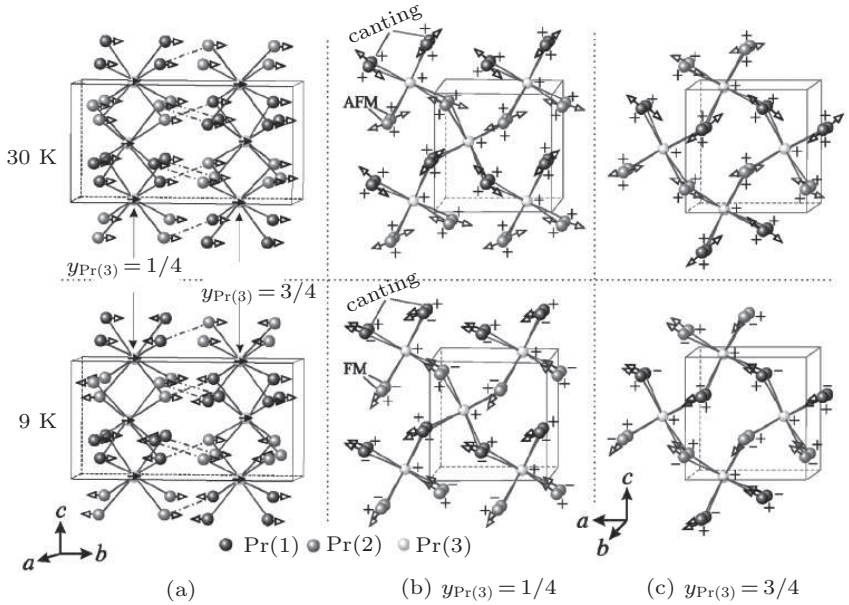


Fig. 24. Magnetic structure models for Pr_5Ge_4 at 30 K and 9 K. (a) Arrangements of the *b* components (arrows) of the Pr magnetic moments. (b) and (c) Arrangements of the Pr magnetic components in the *ac* plane (arrows) and the *b* components (+ and –).[82]

Table 9. Crystallographic data and magnetic moments of Pr_5Ge_4 at room temperature, 50 K, 30 K, and 9 K derived from refinements of the high-resolution neutron diffraction data.

	9 K[a)]	9 K	30 K	50 K	300 K
a/Å	7.9099(2)	7.9105(2)	7.9114(2)	7.9117(3)	7.9172(4)
b/Å	15.1441(5)	15.1455(3)	15.1404(3)	15.1409(7)	15.1916(7)
c/Å	7.9968(3)	7.9973(3)	7.9966(2)	7.9943(3)	8.0112(4)
V (Å^3)	957.92(7)	958.15(4)	957.84(3)	957.64(7)	963.55(8)
Ge (4*c*): *x*	0.9088(4)	0.9096(4)	0.9102(4)	0.9098(4)	0.9121(4)
y	1/4	1/4	1/4	1/4	1/4
z	0.1081(4)	0.1078(4)	0.1075(4)	0.1083(4)	0.1079(4)
$100U_{iso}$	0.33(7)	0.58(7)	0.53(7)	0.44(8)	0.92(7)
Ge (4*c*): *x*	0.1781(4)	0.1786(4)	0.1784(4)	0.1771(4)	0.1784(4)
y	1/4	1/4	1/4	1/4	1/4
z	0.6300(4)	0.6300(4)	0.6308(4)	0.6313(4)	0.6313(4)
$100U_{iso}$	0.16(7)	0.17(7)	0.28(7)	0.26(8)	1.07(8)
Ge (8*d*): *x*	0.2224(3)	0.2222(3)	0.2228(3)	0.2224(3)	0.2209(3)
y	0.9541(1)	0.9541(1)	0.9546(1)	0.9547(2)	0.9554 (2)
z	0.5291(3)	0.5291(3)	0.5296(3)	0.5304(3)	0.5320(3)
$100U_{iso}$	0.22(5)	0.34(4)	0.24(5)	0.25(5)	0.99(5)
Pr(1) (8*d*): *x*	0.1163(4)	0.1164(4)	0.1158(4)	0.1166(5)	0.1196(5)
y	0.1139(2)	0.1141(2)	0.1143(3)	0.1139 (3)	0.1147(3)
z	0.3376(5)	0.3368(5)	0.3372(5)	0.3375(5)	0.3370(5)
$100U_{iso}$	0.0	0.0	0.04(8)	0.40(9)	0.90(9)

Table 9. (*Continued*).

	9 K[a)]	9 K	30 K	50 K	300 K
μ_x/μ_B	2.50(6)	2.40(6)	0.61(6)		
μ_y/μ_B	0.33(5)	0.40(5)	0.58(7)		
μ_z/μ_B	–0.79(5)	–0.87(5)	–0.44(13)		
μ/μ_B	2.64(6)	2.58(5)	0.95(8)		
Pr(2) (8*d*): *x*	0.9721(5)	0.9717(4)	0.9726(5)	0.9745(5)	0.9787(5)
y	0.1007(2)	0.1006(2)	0.1003(2)	0.1008(3)	0.1007(3)
z	0.8192(5)	0.8195(5)	0.8202(5)	0.8201(5)	0.8190(6)
$100U_{iso}$	0.0	0.0	0.21(8)	0.12(9)	0.89(9)
μ_x/μ_B	2.26(5)	2.13(5)	–0.11(6)		
μ_y/μ_B	–0.33(5)	–0.40(5)	0.26(9)		
μ_z/μ_B	1.42(5)	1.48(5)	–0.16(14)		
μ/μ_B	2.69(6)	2.63(5)	0.32(11)		
Pr(3) (4*c*): *x*	0.2860(7)	0.2860(7)	0.2862(7)	0.2855(8)	0.2870(9)
y	1/4	1/4	1/4	1/4	1/4
z	–0.0005(6)	–0.0004(6)	0.0020(5)	0.0041(6)	0.0022(7)
$100U_{iso}$	0.0	0.0	0.26(10)	0.08(11)	1.07(12)
μ_x/μ_B	0.50(7)	0.0	0.0		
μ_y/μ_B	2.69(7)	2.66(7)	2.71(7)		
μ_z/μ_B	–0.28(8)	0.0	0.0		
μ/μ_B	2.75(7)	2.66(7)	2.71(7)		
$R_p(\%)/R_{wp}(\%)/\chi^2$	3.83/4.56/1.048	4.21/4.70/1.083	3.55/4.13/0.945	4.15/4.67/0.948	3.51/4.07/0.885

[a)] Refinement results of the magnetic structural model with symmetry $P112_1'/a'$, in which the Pr atoms on the 8*d* site (x,y,z) in *Pnma* are split into two 4*e* sites in $P112_1/a$: (x,y,z) and $(x, -y+1/2, z)$ with moments (μ_x, μ_y, μ_z) and $(\mu_x, -\mu_y, \mu_z)$, respectively, whereas the Pr on the 4*c* site in *Pnma* occupy the 4*e* site in $P112_1/a$ with fixed $y = 1/4$ and its moment follows the $P112_1'/a'$ symmetry. For the sake of comparison, the site symbol 8*d* is retained in the table.

2.3. $Gd_{5-x}La_xGe_4$

Crystal structures of three representative compounds, Gd_5Ge_4, La_5Ge_4, and $Gd_3La_2Ge_4$, were studied by XRD at room temperature,[83] showing that Gd_5Ge_4 and La_5Ge_4 crystallize in the orthorhombic Sm_5Ge_4-type structure with space group *Pnma*. The ternary intermediate compound $Gd_3La_2Ge_4$ crystallizes in the monoclinic $Gd_5Si_2Ge_2$-type structure with space group $P112_1/a$. Figure 25 shows the experimental and calculated XRD patterns of these compounds. The lattice and atomic parameters are listed in Tables 10 and 11.

Table 10. Crystal structure data of Gd_5Ge_4, $Gd_3La_2Ge_4$, and La_5Ge_4.

	Gd_5Ge_4	$Gd_3La_2Ge_4$	La_5Ge_4
Space group	*Pnma*	$P112_1/a$	*Pnma*
a/Å	7.6890(1)	7.7486(2)	8.0761(1)
b/Å	14.8196(2)	15.0729(4)	15.5209(3)
c/Å	7.7800(1)	7.9648(3)	8.1725(1)
V/Å^3	886.51	929.5	1024.41
γ/(°)	90	92.29(0)	90
R_p/%	8.14	7.25	8.25
R_{wp}/%	10.91	9.46	10.76
R_{exp}/%	3.81	3.68	3.91

Table 11. Atomic parameters of Gd_5Ge_4, $Gd_3La_2Ge_4$, and La_5Ge_4.

Atom	*x*/*a*	*y*/*b*	*z*/*c*
Gd_5Ge_4			
Gd1 (4*c*)	0.2927(7)	0.25	0.0022(7)
Gd2 (8*d*)	–0.0237(4)	0.0997(2)	0.1811(5)
Gd3 (8*d*)	0.3787(4)	0.8821(2)	0.1629(5)
Ge1 (4*c*)	0.1712(10)	0.2500	0.3688(12)
Ge2 (4*c*)	0.9157(11)	0.2500	0.8840(11)
Ge3 (8*d*)	0.2180(9)	0.9553(4)	0.4730(8)
$Gd_3La_2Ge_4$			
*M*1[a)] (4*e*)	0.3312(10)	0.2486(5)	0.0074(7)
*M*2a (4*e*)	–0.0056(8)	0.0988(4)	0.1864(9)
*M*2b (4*e*)	0.0098(7)	0.3996(4)	0.1676(10)
*M*3a (4*e*)	0.3523(7)	0.8810(4)	0.1678(9)
*M*3b (4*e*)	0.3310(9)	0.6230(4)	0.1748(9)
Ge1 (4*e*)	0.1913(16)	0.2470(9)	0.3730(12)
Ge2 (4*e*)	0.9508(14)	0.2557(8)	0.8726(4)
Ge3a (4*e*)	0.2094(17)	0.9556(7)	0.4604(15)
Ge3b (4*e*)	0.1646(15)	0.5418(7)	0.4616(14)
La_5Ge_4			
La1 (4*c*)	0.2950(6)	0.2500	0.0000(6)
La2 (8*d*)	–0.0195(4)	0.1034(2)	0.1824(4)
La3 (8*d*)	0.3781(4)	0.8881(2)	0.1613(4)
Ge1 (4*c*)	0.1709(10)	0.2500	0.3612(11)
Ge2 (4*c*)	0.9103(11)	0.2500	0.8954(10)
Ge3 (8*d*)	0.2196(8)	0.9510(3)	0.4677(8)

[a)] *M* = (0.6Gd+0.4La)

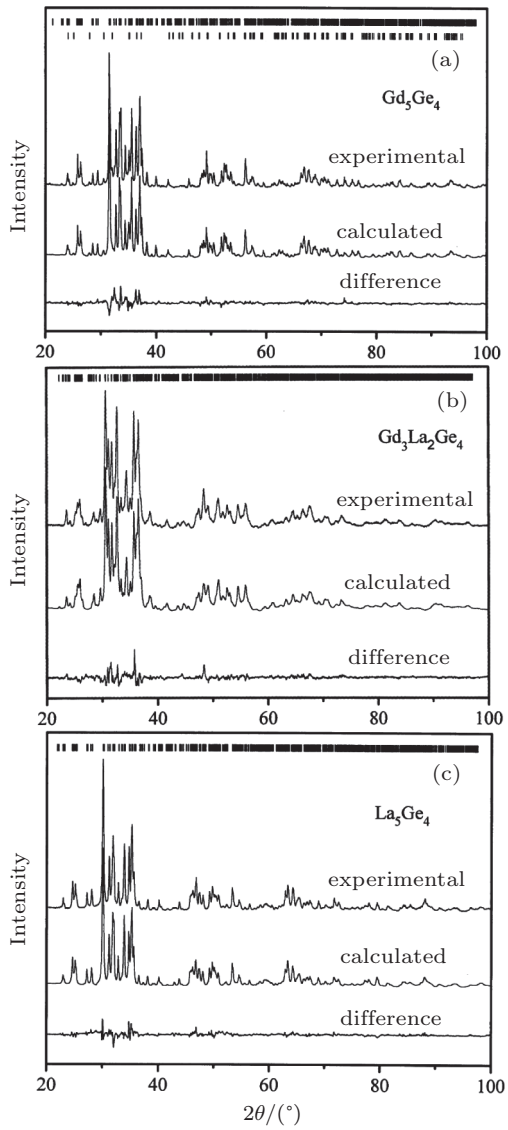


Fig. 25. Experimental and calculated XRD patterns of (a) Gd_5Ge_4, (b) $Gd_3La_2Ge_4$, and (c) La_5Ge_4, and the differences between them. The vertical bars indicate the expected Bragg reflection positions.[83]

2.4. La_5Si_4 and Gd_5Sn_4

Other compounds studied include La_5Si_4[68] and Gd_5Sn_4.[84–86] The crystal structure of La_5Si_4 was studied by XRD at room temperature, as shown in Fig. 26. It crystallizes in the tetragonal Zr_5Si_4-type structure with space group $P4_12_12$. From the profile fitting of the powder diffraction pattern by the Rietveld method, the lattice parameters of La_5Si_4 are a= 8.0467(0) Å and c= 15.4476(1) Å. The detailed atomic parameters are reported in Ref. [68].

Ryan and coworkers[85,86] reported giant MCE in Gd_5Sn_4 with the Sm_5Ge_4-type structure. It was thus expected that, like $Gd_5(Si_xGe_{1-x})_4$, the compound undergoes a structural transition at T_C ~80 K between two closely related orthorhombic forms (the orthorhombic Sm_5Ge_4-type and Gd_5Si_4-type structures).[37] However, the temperature dependent XRD revealed that there is no structural transition around the temperature at which the first-order magnetic transition occurs, i.e., the compound retains the Sm_5Ge_4-type structure from 80 K ($< T_C$) to 298 K ($> T_C$).[84] Figure 27 shows the XRD patterns at 80 K and 298 K.

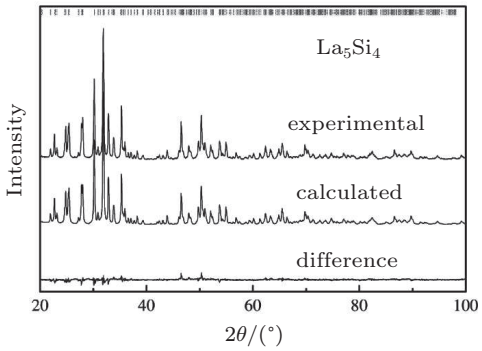


Fig. 26. Experimental and calculated XRD patterns of La_5Si_4 and the difference between them. The vertical bars indicate the expected Bragg reflection positions.[68]

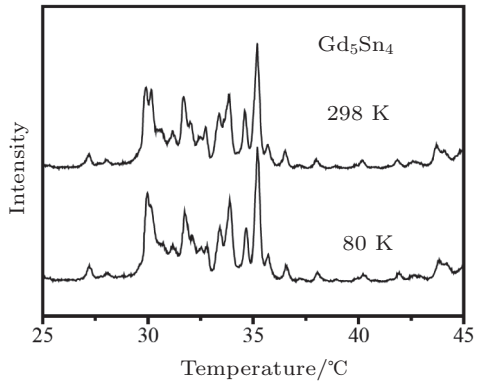


Fig. 27. XRD patterns of Gd_5Sn_4 at 80 K and 298 K.[84]

3. Phase relationship and magnetic transitions of $Gd_5(Si,Ge)_4$ alloys

3.1. Completely miscible solid solution in $Gd_5(Si_{1-x}Ge_x)_4$

The temperature dependence of magnetization of $Gd_5(Si_{1-x}Ge_x)_4$ was investigated and T_C was found to decrease with increasing x. The temperature-dependent XRD[87] revealed that all compounds crystallize in the Gd_5Si_4-type O(I) structure below T_C regardless of the composition and the crystal structure above T_C. Figure 28 shows the concentration dependences of both the lattice parameters (a, b, c) and unit cell volume of $Gd_5(Si_{1-x}Ge_x)_4$ at 80 K and 298 K. The parameters reported by Pecharsky *et al.*[29] are also shown for comparison. It is well known that above T_C, the alloy system is composed of three partially miscible solid solutions, i.e., Gd_5Si_4 based ($x < 0.5$), Gd_5Ge_4-based ($x \geq 0.8$), and $Gd_5Si_2Ge_2$ ($0.5 \leq x < 0.8$) based solid solutions. However, the lattice constants at 80 K are those of the Gd_5Si_4-type O(I) structure and all these parameters exhibit a linear increase in the range of $0.0 \leq x \leq 0.85$, in accordance with the Vegard's law. This indicates that the $Gd_5(Si_{1-x}Ge_x)_4$ compounds form a completely miscible solid solution with the

Gd_5Si_4-type structure at low temperature, which is rather intriguing. Usually, a completely miscible solid solution forms at high temperature and decomposes into a partially miscible solid solution at low temperature. This unusual feature in $Gd_5(Si_{1-x}Ge_x)_4$ can be understood by taking into account the competing effects of the FM exchange interaction and the lattice strain in the solid solution. Based on temperature dependent XRD and magnetization measurements, a crystallographic and magnetic phase diagram of $Gd_5(Si_{1-x}Ge_x)_4$ is constructed and shown in Fig. 29. In this system, the temperature of the structural phase transition always coincides with T_C and the FM state of the compound occurs exclusively in the Gd_5Si_4-type O(I) structure.

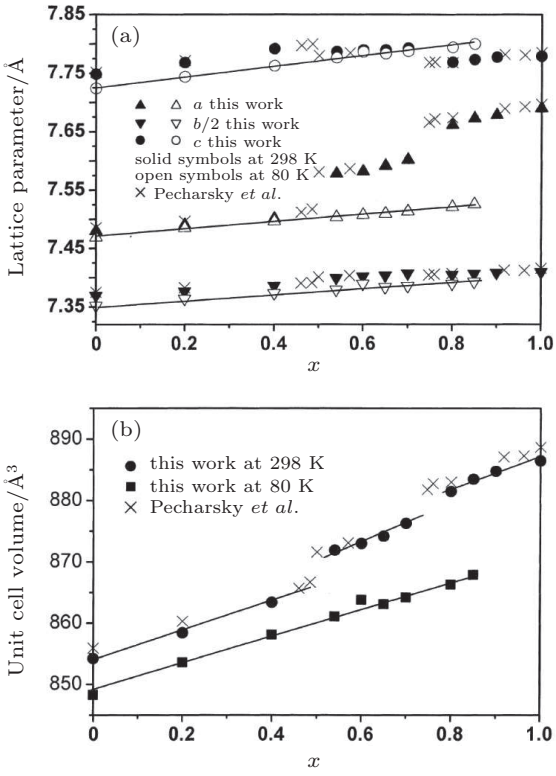


Fig. 28. The x dependences of (a) lattice parameters and (b) unit cell volume of $Gd_5(Si_{1-x}Ge_x)_4$. The lines are guides for the eye.[87]

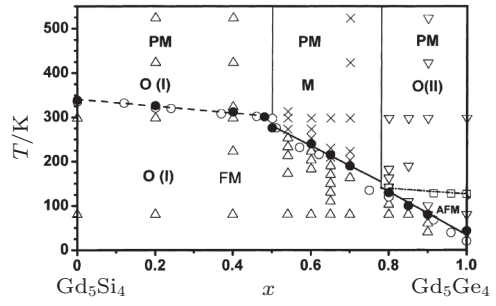


Fig. 29. The T–x phase diagram of $Gd_5(Si_{1-x}Ge_x)_4$, here • stands for T_C of this work, ◯ for T_C from Ref. [29], □ for T_N from Ref. [29], △ for Gd_5Si_4-based phase O(I), ∇ for Gd_5Ge_4-based phase O(II), × for monoclinic phase M. The solid lines depict crystallographic phase boundaries. The dashed lines depict the magnetic phase boundaries.[87]

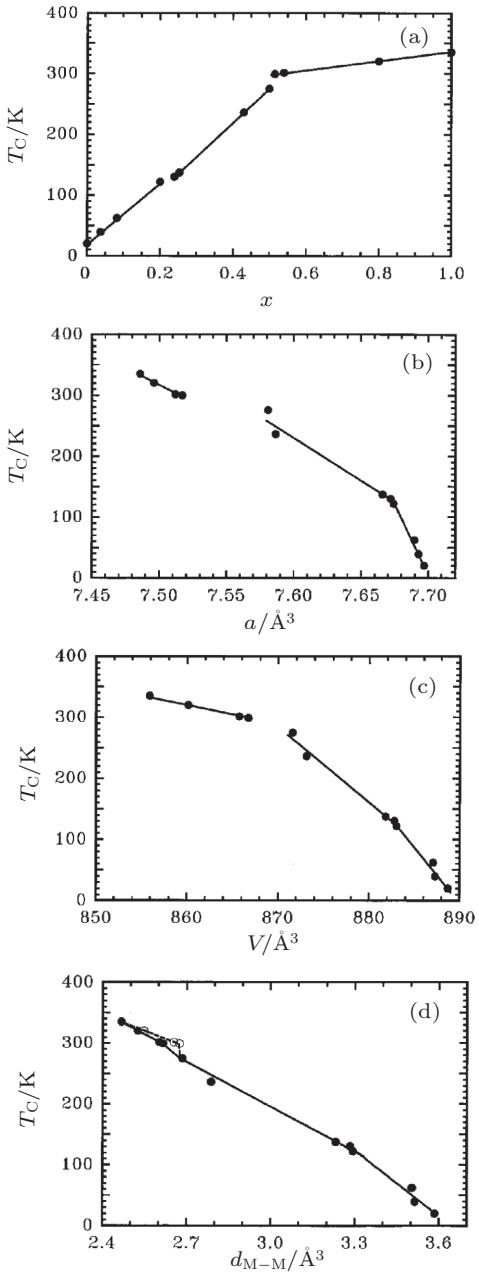


Fig. 30. The T_C as a function of (a) x, (b) lattice parameter a, (c) unit cell volume V, and (d) the M–M bond length in $Gd_5(Si_xGe_{1-x})_4$.[88]

By analyzing the variation of M–M bond length d_{M-M} (M = Si, Ge, or a mixture of Si and Ge) with x for the reported crystal structure of the $Gd_5(Si_xGe_{1-x})_4$ compounds, a possible correlation between the crystal structure and magnetic properties of the compounds is explored.[88] Figure 30 shows the FM ordering temperature T_C as a function of x, lattice parameter a, unit cell volume V, and the M–M bond length. An almost linear dependence of T_C on the M–M bond length is derived within the first approximation. It has been proposed that the mechanism of the FM coupling in both the Gd_5Si_4-based ($x > 0.5$) and the Gd_5Ge_4-based ($x \leq 0.2$) solid solutions is the same as that in the intermediate phase with $0.24 \leq x \leq 0.5$, in which the FM Gd-(Gd,M)-Gd blocks couple with each other via an M_2 layer regardless of their crystal structure at room

temperature. The orthorhombic structure of the intermediate phase at low temperature is stabilized by the FM exchange interaction, which compensates the increase of the strain energy when the O(II) or M structure transforms to the O(I) structure and leads to the formation of the completely miscible solid solution at low temperature.

3.2. Gd_5Ge_4 — an amazing material

Gd_5Ge_4 is an especially interesting material in the family of giant magnetocaloric $Gd_5(Si_{1-x}Ge_x)_4$. In addition to the strong magnetocaloric and thermal effects,[89] many novel magnetic properties, such as unusual training effect,[41] phase separation,[90] glass-like kinetically arrested state,[45] frozen magnetostructural order,[28] and magnetic deflagration,[91] have been revealed in the past few years. Gd_5Ge_4 is AFM below T_N= 128 K,[92] as confirmed by X-ray resonant magnetic-scattering measurements.[93] This AFM ground state can be transformed into FM state by magnetic field and pressure, which is accompanied by a simultaneous change in the crystal structure of the compound.[37,94] Generally, the AFM–FM transition is fully irreversible below ~10 K, partially reversible between ~10 K and ~20 K, and completely reversible above ~20 K.[92,95] It is believed that the novel magnetic behavior observed in Gd_5Ge_4 is closely related with this first-order AFM–FM magnetostructural transition. In this subsection, we summarize several intriguing magnetic properties, showing that Gd_5Ge_4 is an amazing material.

3.2.1. Magnetic anisotropy

The magnetic anisotropy first manifests in the AFM state, where the magnetization in the zfc $M(H)$ process increases nearly linearly with the applied field along the a or b axis in low fields, but the magnetic behavior along the c axis is quite different.[96] Figure 31 shows the zfc $M(H)$ curves of a Gd_5Ge_4 single crystal measured along the c axis. A spin-flop transition is observed, showing that the AFM coupling of Gd moments occurs along the c axis (the Gd moments within each slab couple ferromagnetically). Figure 32 shows the temperature dependence of the spin-flop transition. The critical field H_{sf} increases as the temperature increases until the disappearance of the spin-flop transition at T_N. Above this temperature, the low-field $M(H)$ curves are identical for all the three axes, implying the absence of the AFM anisotropy. Figure 33 shows zfc heating and fc $M(T)$ curves of the single crystal. The c axis curve below T_N is characterized by the spin-flop transition, which diminishes with the increasing field, similar to the effect of temperature. The anisotropic behavior in the AFM state is due to the variation of magnetization energy between the c axis and the a or b axis of the orthorhombic crystal caused by a different alignment of the Gd moments with respect to the magnetic field direction.

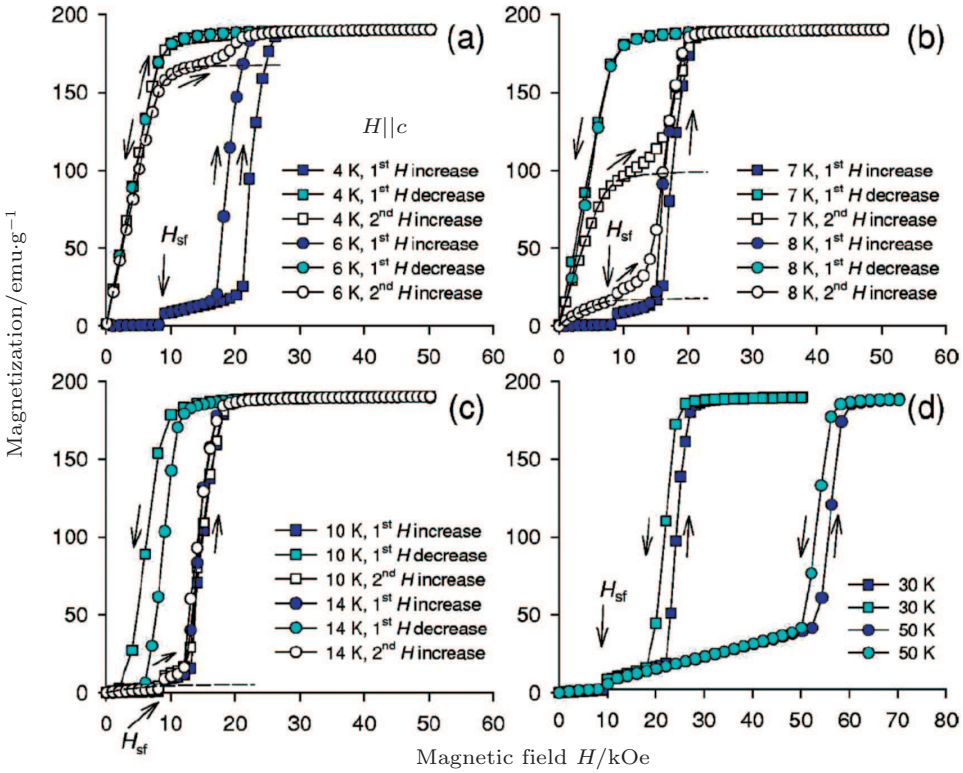


Fig. 31. The zfc $M(H)$ curves of single crystal of Gd_5Ge_4 measured along the c axis. Panels (a)–(d) show results at different temperatures. The dashed lines show the extrapolated magnetic behavior without the magnetic field-induced AFM–FM transition during the second field-increasing measurement. The arrows marked H_{sf} point to the anomalies associated with a spin-flop transition.[96]

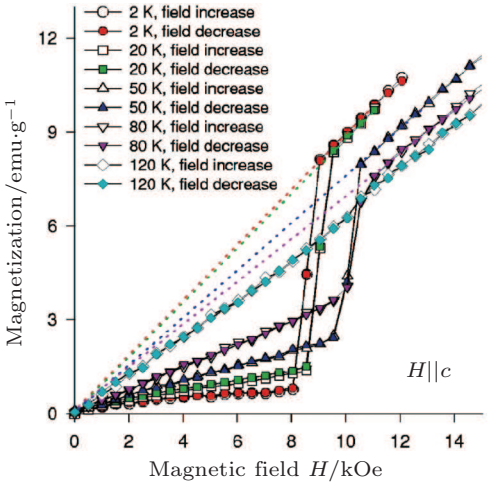


Fig. 32. Temperature dependent spin-flop transition along the c axis of Gd_5Ge_4. The dotted lines represent linear extrapolations of the $M(H)$ behavior above the spin-flop transition to a zero magnetic field.[96]

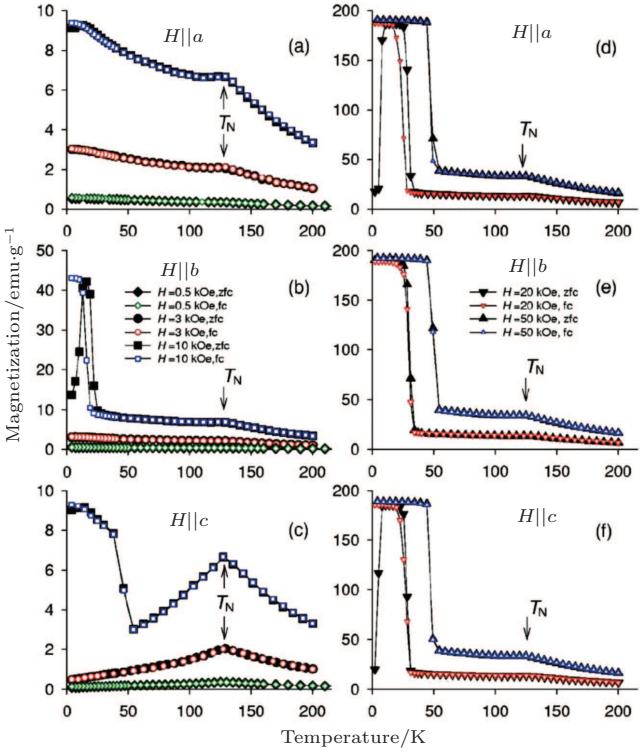


Fig. 33. The zfc heating (solid points) and fc (open points) $M(T)$ curves of Gd_5Ge_4 measured at $H = 0.05$ T, 0.3 T, 1 T ((a)–(c)) and $H = 2$ T, 5 T ((d)–(f)).[96]

The field-induced magnetostructural transition is also anisotropic. The critical magnetic field for the AFM–FM transition is the smallest when the magnetic field is parallel to the b axis, indicating an easy magnetization direction along this axis. The anisotropy of the magnetic field-induced magnetostructural transformation in Gd_5Ge_4 is obviously associated with the coupled magnetic and structural transitions. Anisotropic magnetic phase diagrams along the three major crystallographic axes are constructed as shown in Fig. 34. The left panels are derived from the initial magnetization of the zfc sample and the right panels from the second isothermal magnetization of the sample. As in the polycrystalline sample, T_N slowly decreases with increasing magnetic field. The critical fields H_{c1} and H_{c2} associated with the start and the end of the AFM–FM transition, respectively, first decrease and then increase with increasing temperature. Both exhibit a minimum around 14 K for the three axes. An extrapolation of the curves, shown by the dashed lines in Fig. 34, results in a tricritical point with $H_{tcr} = 14$ T, above which the AFM state is completely suppressed, and $T_{tcr} = 90$ K.

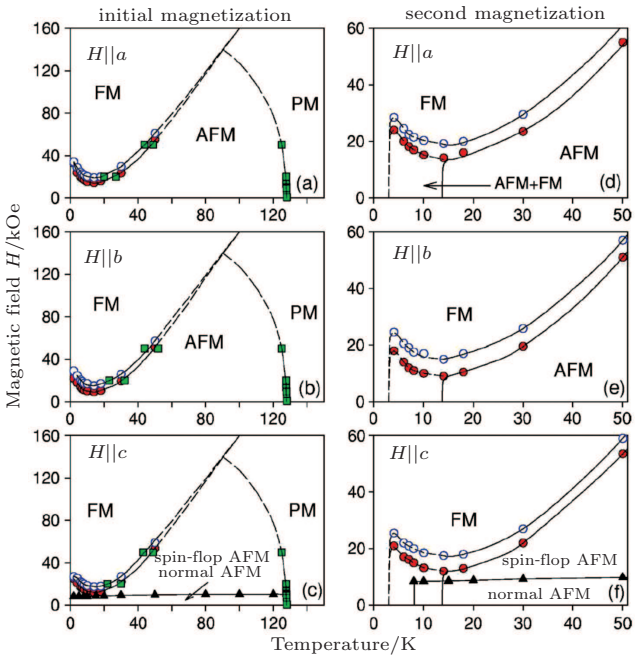


Fig. 34. The H–T magnetic phase diagrams of Gd_5Ge_4 along the three principal crystallographic axes, in which the dots (•) and (◯) are the critical fields H_{c1} and H_{c2}, respectively, obtained from the $M(H)$ curves, the squares (■) are the data derived from the $M(T)$ curves, and the triangles (▲) are the data of H_{sf}. Panels (a)–(c) are for the initial magnetization of the zfc single crystal. The dashed lines are extrapolations for magnetic field exceeding 5 T. Panels (d)–(f) are for the second magnetization with only the low-temperature parts shown for clarity because above ∼ 14 K the initial magnetization and the second magnetization diagrams are indistinguishable for the same direction.[96]

3.2.2. Angular dependence of the spin-flop transition

Although the spin-flop transition along the c axis is observed in both the $M(H)$ and $M(T)$ curves of Gd_5Ge_4, its nature is less understood. In fact, as early as 1936, Néel[97] predicted that in a uniaxial anisotropic antiferromagnet where the magnetic moments couple with the crystal lattice, a first-order spin-flop transition should occur at a certain critical magnetic field H_{sf} when the magnetic field is applied along the AFM coupling direction, i.e., along the AFM easy axis. As a result of the spin-flop transition, the directions of the spin moments of the two sublattices abruptly change from their antiparallel configuration in which the moments are collinear with the external field, to a new spin-flop configuration in which the moments remain antiparallel but become nearly perpendicular to the magnetic field vector. The spin-flop transition has been experimentally observed in $CuCl_2{\cdot}2H_2O$,[98] MnF_2,[99] FeF_2,[100] and low dimensional systems.[101]

For Gd_5Ge_4, the Gd moments couple ferromagnetically within the slabs, while the Gd moments between the slabs couple antiferromagnetically along the c axis, thus showing that the zfc Gd_5Ge_4 is a uniaxial antiferromagnet, as shown in Fig. 35.[102] Levin *et al.*[103] suggested that in the spin-flop state, the AFM coupling axis coincides with the a axis, which is logical considering that the moments then have to rotate in the planes of the slabs rather than out of the planes of the slabs. The AFM coupling axis is perpendicular to the field vector in the spin-flop phase, but the magnetization of each sublattice is slightly tilted away from the spin coupling axis (a axis) due to the application of the magnetic field. However, this model has not been verified experimentally.

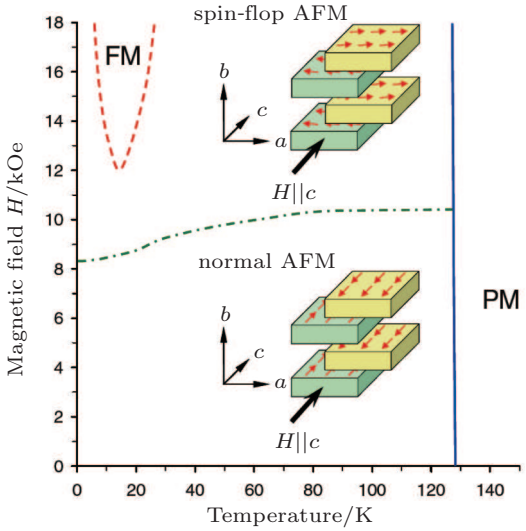


Fig. 35. The H–T phase diagram for the spin-flop transition of Gd_5Ge_4. This diagram is for the initial magnetization of the zfc sample with the magnetic field vector parallel to the c axis.[102]

In a uniaxial antiferromagnet, where the anisotropic energy is usually small compared to the generally isotropic exchange energy, the first-order spin-flop transition can be observed only over a small range of tilt angles when the field vector remains perpendicular to the hard axis but is tilted away from the AFM easy axis toward the next easiest axis, i.e., toward the spin-flop axis.[98] Figures 36 and 37 show the field dependence of the magnetization of single crystal Gd_5Ge_4 measured at 2 K while the field vector gradually tilts away from the c axis toward the b axis (the cb plane isotherms) and away from the c axis toward the a axis (the ca plane isotherms).[102] The first-order spin-flop transition is always observed in the cb plane isotherm $M(H)$ curves, but within only a small range of angles in the ca plane isotherm $M(H)$ curves. These experiments seem to corroborate the earlier prediction by Levin *et al.*[103] that the microscopic magnetic structure of the spin-flop AFM phase is the result of rotating the AFM coupled moments in the ac plane, as shown schematically in Fig. 35, rather than in the ab plane. The range of tilt angles in Gd_5Ge_4 is comparable to that of other uniaxial antiferromagnets exhibiting the spin-flop transition and their differences can be understood by considering the competition between anisotropic energy and isotropic exchange energy.

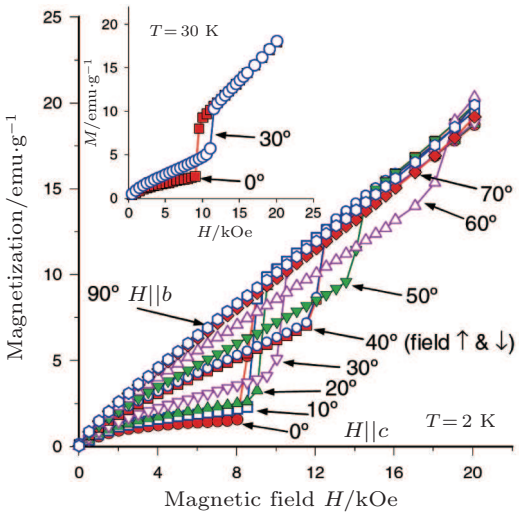


Fig. 36. The $M(H)$ curves at 2 K for Gd_5Ge_4 with the magnetic field vector gradually tilted away from the c axis toward the b axis (the cb plane isothermals). The inset shows two isothermals measured at $T = 30$ K with $H||c$ and with $H\angle c = 30°$ in the cb plane.[102]

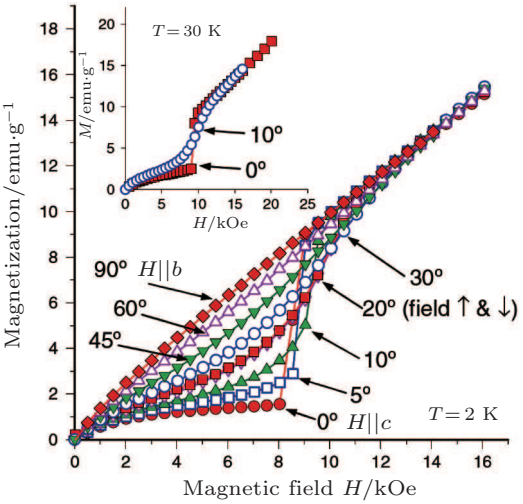


Fig. 37. The $M(H)$ curves at 2 K for Gd_5Ge_4 with the magnetic field vector gradually tilted away from the c axis toward the a axis (the ca plane isothermals). The inset shows two isothermals measured at $T = 30$ K with $H||c$ and with $H\angle c = 10°$ in the ca plane.[102]

3.2.3. Metastable magnetic response across the AFM–FM transition

Metastable magnetic response across the AFM–FM transition in Gd_5Ge_4 was first investigated by Hardy *et al.*,[90] who found that the field-sweep rate (dH/dt) dependence of the magnetization $M(H)$ is related to the martensitic character of the structural transformation accompanying the AFM–FM transition. This unusual magnetic dynamics is also expected to be observed in single crystal Gd_5Ge_4, the details of which are briefly described as follows.[104]

First, at low temperatures, the critical magnetic fields for both the onset and the completion of the AFM–FM transformation, H_{c1} and H_{c2}, respectively, depend on the size of the magnetic-field step (ΔH) employed during isothermal $M(H)$ measurements: the smaller the step, the lower the critical field, as shown in Fig. 38. This feature is common for different single crystal samples S1 and S2. This occurs due to the progressively better accommodation of the martensitic strains. As ΔH decreases, the system resides in the fields close to critical for a longer time, and therefore, has enough time for the nucleation and growth of the FM phase even when $H < H_{c1}$ (also see magnetic relaxation data below). The dependencies of H_{c1} on ΔH for three different single crystalline samples are shown in Fig. 39. All curves exhibit a logarithmic variation with the size of the field step. Even though the observed critical fields differ from one sample to another, they appear to collapse to the same value of $2.4T < H_{c1} < 2.5$ T as $\Delta H \to 0$. This behavior indicates that the slower the measurement, the closer the sample is brought to equilibrium. It also suggests that different single crystals have different strain fields due to possible variations in mosaicity and other factors related to their microstructures, such as details of their twin structures[36] and the concentrations of Gd_5Ge_3 platelets.[105]

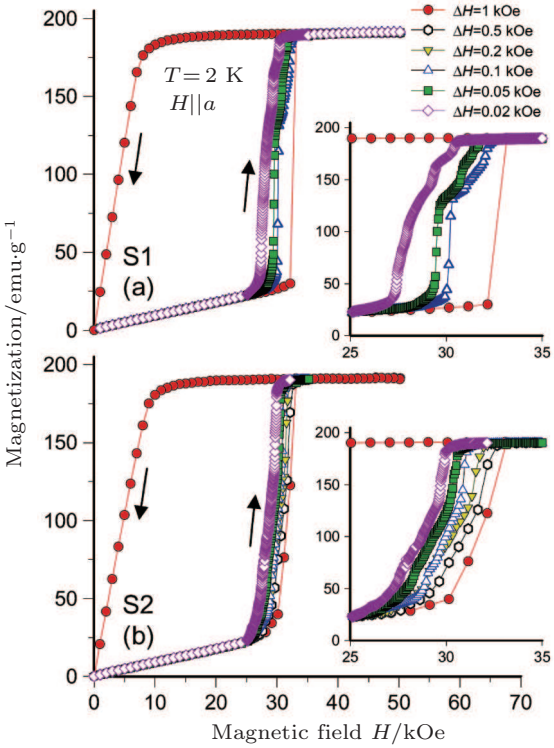


Fig. 38. Isothermal $M(H)$ curves for the a axis of two different Gd_5Ge_4 single crystals ((a) S1 and (b) S2) measured at 2 K after zero field cooling from 300 K. The insets clarify details of the AFM–FM transitions.[104]

Second, as the temperature rises, the effect of the magnetic-field step size on the magnetostructural transition in Gd_5Ge_4 becomes smaller and the shift of H_{c1} (and H_{c2}) almost disappears at 30 K, which can be seen from the $M(H)$ curves (Fig. 40). In a second magnetization process, additional broad FM steps are observed between 4 K and 14 K (see the T=7 K curves, Fig. 40(b)). These steps reflect the residual FM phase remaining in the sample after the first magnetization-demagnetization cycle due to the kinetic retardation and the resulting incomplete reversibility of the transformation. The second magnetization curve also reveals a shift of H_{c1} during the transition when ΔH is reduced to 0.005 T.

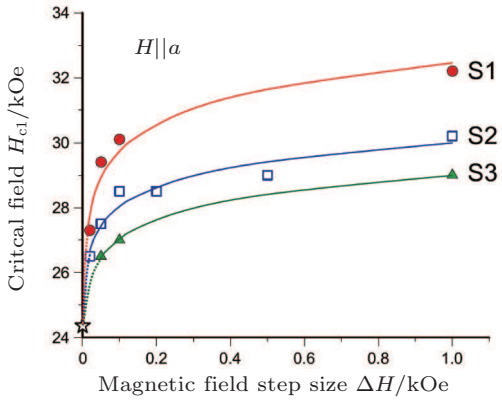


Fig. 39. Critical fields H_{c1} of the a axis for different Gd_5Ge_4 samples (S1–S3) as functions of the magnetic-field step size measured at $T = 2$ K. The solid lines are logarithmic fits of the data. The dotted lines represent an estimated common H_{c1} (shown as a star) when ΔH approaches zero.[104]

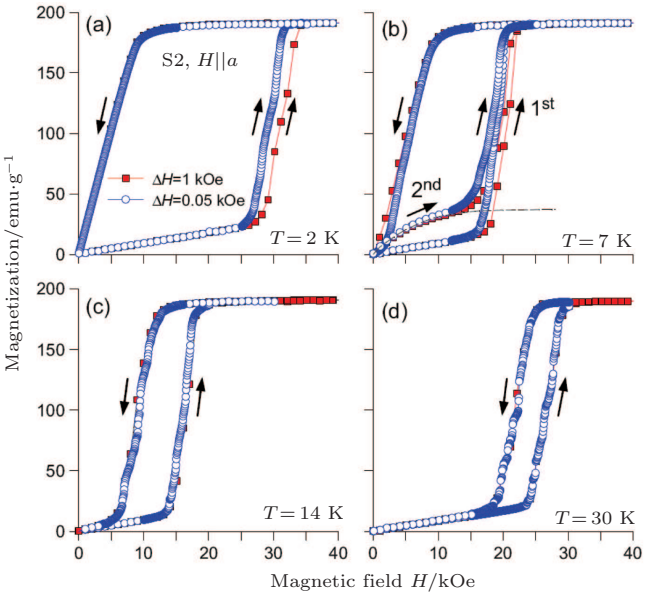


Fig. 40. Isothermal $M(H)$ curves for the a axis measured at (a) 2 K, (b) 7 K, (c) 14 K, and (d) 30 K with $\Delta H = 0.1$ T and 0.005 T for single crystal of Gd_5Ge_4 (S2). In all cases except for the second measurement in panel (b), the sample is zero-field cooled from 300 K to 2 K and then warmed to the temperature of measurement. The second measurement in panel (b) is performed isothermally immediately following the first magnetization and demagnetization of the specimen. The arrows show the direction of the magnetic-field change.[104]

Third, weakening of the field step size effect suggests that the magnetization relaxation across the magnetostructural transformation is suppressed with the increase of temperature. Figure 41 shows the magnetization relaxation curves of S2

measured with the magnetic field parallel to the a axis at different temperatures during both the magnetization and demagnetization. With increasing temperature, the relaxation gradually weakens, and practically disappears at 30 K. The magnetic relaxation curves shown in Fig. 41 also exhibit several steps, some of which are indicated by the arrows in the figure. The steps observed from 2 K to 9 K are smooth but those appearing above 14 K become sharper. A close examination of the $M(t)$ behavior reveals that the relaxation data at 20 K and 30 K exhibit several discontinuous steps as shown in Fig. 42, and the magnetization changes very slowly before and after each of the steps. Irreproducibility indicates that these steps are stochastic (thermally activated). Details of these features are described in Ref. [104]. Similar phenomena are expected to occur in other martensitic-like systems, e.g., the manganites.

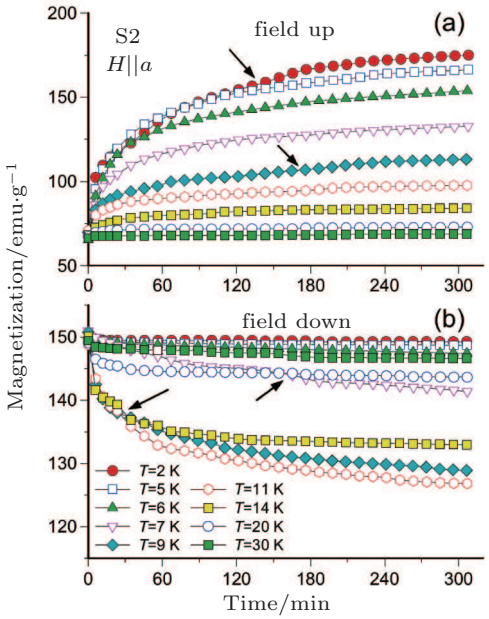


Fig. 41. Time evolution of the magnetization for the a axis of Gd_5Ge_4 (S2) with a fixed magnetic field between H_{c1} and H_{c2}. The arrows point to some of the observed magnetization steps.[104]

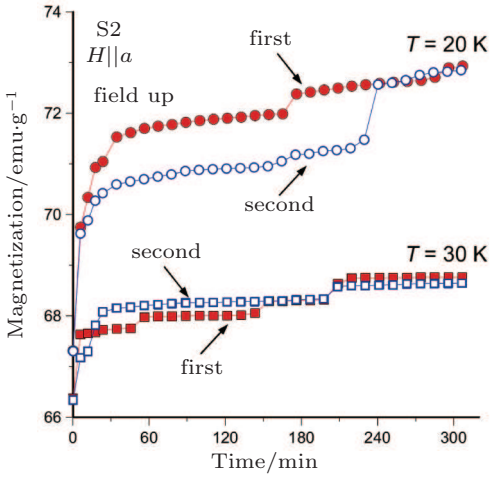


Fig. 42. Time evolution of the magnetization for the a axis of Gd_5Ge_4 (S2) measured at 20 K and 30 K repeatedly at the same fixed magnetic field located between H_{c1} and H_{c2}.[104]

3.2.4. Griffiths-like phase

The Griffiths phase (GP) is a peculiar magnetic state in which the magnetization fails to be an analytical function of the magnetic field H between T_C and T_G when H approaches zero, where T_C is the conventional long range FM ordering temperature (Curie temperature) and T_G represents the onset of completely random magnetic interactions (true paramagnetism). This phenomenon was first predicted to occur in randomly diluted Ising ferromagnets[106] and latter in various systems.[50,107] The appearance of the Griffiths phase is usually associated with competing magnetic interactions leading to FM clustering, the origin of which may differ from one material to another.

In Gd_5Ge_4, the GP-like phase manifests as an unusually large hysteresis and anomalies of the dc and ac magnetic susceptibilities in low magnetic fields.[32] Figure 43 displays the inverse magnetic susceptibility (H/M) curves of single crystal Gd_5Ge_4. The 0.5 T data follow the Curie–Weiss law above ~ 170 K for all the three axes with a common PM Curie temperature, $\theta_P = 100$ K (showing a strong FM coupling within the slabs), and a practically the same effective magnetic moment of 7.89 μ_B/Gd, which is equal to the expected moment for a free Gd^{3+} ion. The low field H/M curves, however, follow the Curie–Weiss law only above $T_G = 240$ K, exhibiting a rapid downturn below this temperature. The lower the field, the larger the negative deviation from the usual PM behavior. Below T_G in zfc heating, fc cooling, and fc heating curves, the magnetic susceptibility along the b axis always exhibits greater deviation than that observed along the a and c axes, indicating that the magnetic susceptibility along the b axis plays a major role in defining the GP-like phase. This observation correlates well with the fact that the magnetic field-induced FM state of Gd_5Ge_4 is most stable when the field is applied along the b axis, which is also the easy magnetization direction of the O(I) FM Gd_5Ge_4 (see Subsection 3.2.1). Hence, the magnetic anisotropy shown in Fig. 43 is consistent with FM clustering, which is controlled by the crystallographic anisotropy of this distinctly layered structure, and it is readily apparent that the b axis component of the magnetization of these clusters is dominant.

The GP-like singularity is characterized by an exponential less than unity, that is, $H/M \sim (T - T_C)^{-(1-\lambda)}$, where $0 \leq \lambda < 1$.[108] The λ_G is found to be highly anisotropic, varying from 0.27 (c axis) to 0.61 (b axis) for $T_N < T < 170$ K (see Fig. 43(d)). It becomes isotropic and zero in the PM state, i.e., $\lambda_{PM} = 0$ for $T_G > 240$ K. Microscopically, the formation of the Griffiths-like phase can be related to the competition of the interslab and intraslab magnetic exchange interactions that are present in a distinctly layered crystal structure of the compound. Macroscopically, the appearance of the Griffiths-like

phase may be enhanced by the precipitates of thin plates of Gd_5Ge_3 present in the sample. Figure 44 shows the updated H–T phase diagram (the b axis) of Gd_5Ge_4, including the presence of the GP-like regime above T_N. Note that in a low field, short-range FM clustering extends into the AFM regime, it is microscopically inequivalent to that occurring above the T_N. We thus designate this phase region as the one with short-range FM clustering (SRFMC).

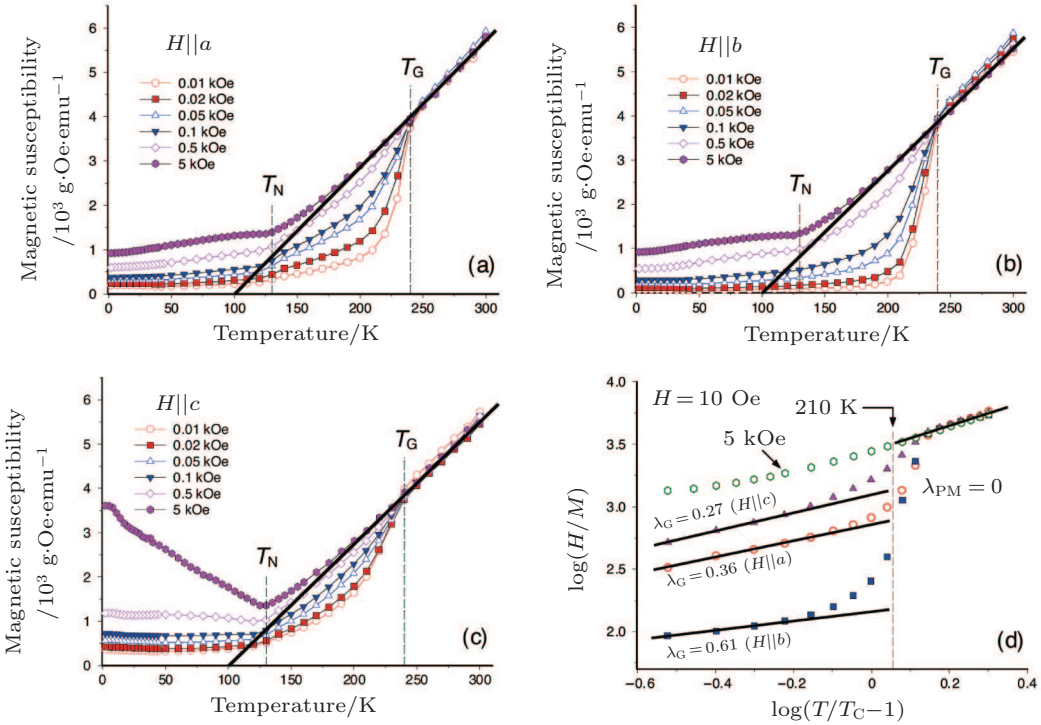


Fig. 43. The fc cooling H/M curves of single crystal Gd_5Ge_4 measured along the (a) a axis, (b) b axis, and (c) c axis in the magnetic fields ranging from 0.001 T to 0.5 T. The solid lines in panels (a)–(c) represent the Curie–Weiss fits of the 0.5 T data. The solid lines in panel (d) are linear fits of $\log(H/M)$ vs $\log(T/T_C - 1)$, with the dashed vertical line indicating the maximum slope of the curve for $H||b$.[32]

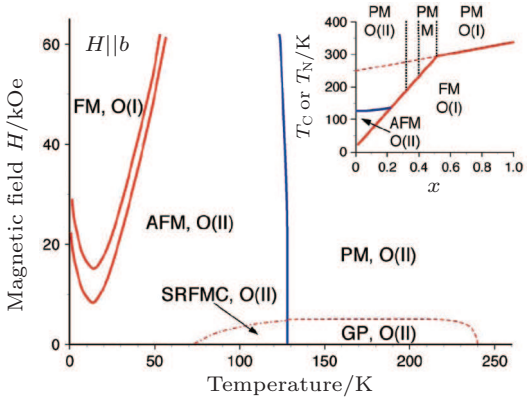


Fig. 44. Refined H–T magnetic phase diagram for the initial magnetization along the b axis of Gd_5Ge_4. The inset shows the extrapolation of the Curie temperature of the Si-rich O(I)-type $Gd_5(Si_xGe_{1-x})_4$.[32]

An extended investigation of $Gd_5(Si_xGe_{1-x})_4$ revealed that the GP-like phase exists within the range of $0 \leq x < 0.5$.[31] Figure 45 shows the concentration dependence of the low-field fc cooling H/M curves. With increasing Si concentration, T_G increases but the negative deviation of H/M from the conventional PM behavior decreases and becomes quite small at $x = 0.375$, implying a reduction in either the size or amount of the FM clusters. When $x = 0.875$, no negative deviation is observed, evidencing the disappearance of the GP-like anomaly. The Griffiths singularity as well as the values of λ_G is shown in Fig. 46. The extrapolation of $\lambda_G(x)$ results in λ_G=0 at $x = 0.5$, suggesting that the GP-like phase is present in the region of $0 \leq x < 0.5$. The low-field GP-like phase and the short-range FM correlations extending into the AFM regime are depicted in the T–x phase diagram of $Gd_5(Si_xGe_{1-x})_4$ (see Fig. 1).

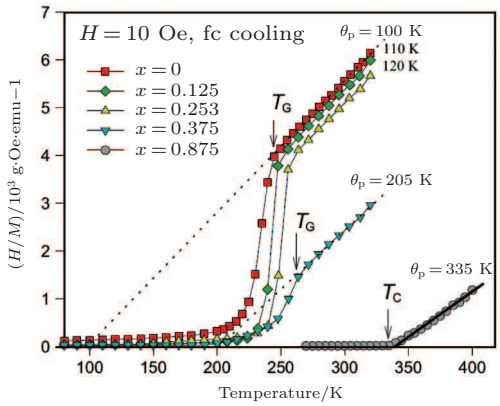


Fig. 45. The fc cooling H/M curves of $Gd_5(Si_xGe_{1-x})_4$ measured at 0.001 T. The dashed lines are Curie–Weiss fits above T_G.[31]

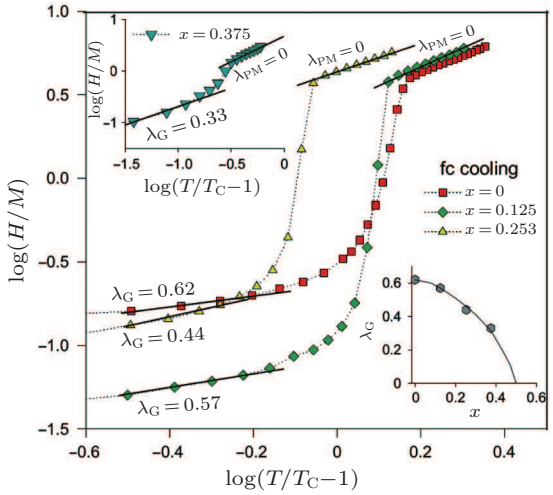


Fig. 46. The fc cooling $\log(H/M)$ vs. $\log(T/T_C - 1)$ curves of $Gd_5(Si_xGe_{1-x})_4$. The solid lines are linear fits of the curves. The inset at the right bottom is the composition x dependence of λ_G.[31]

3.2.5. Magnetostructural transition under pulsed magnetic fields

The field-induced magnetostructural transition in Gd_5Ge_4 described above was in general investigated by the conventional isothermal $M(H)$ measurements in steady magnetic fields. During the magnetization (or demagnetization) process, the temperature of the sample remains nearly constant by exhausting the MCE-related heat into surroundings (or by absorbing the heat from the surroundings). This raises a question regarding the influence of the magnetic field-induced thermal effects on the $M(H)$ measurements performed in quickly varying ultrafast magnetic fields, because the heat exchange between the sample and the surroundings may not be completed fast enough. This issue was well addressed in detailed studies on the magnetostructural transition of Gd_5Ge_4 induced by pulsed magnetic fields.[109]

Figure 47 shows several typical pulsed fields with the same duration but various peak values of $\mu_0 H_{max}$. The magnetic field-sweep rate $\mu_0 dH/dt$ is measured by $\mu_0 H_{max}/t_{max}$, where t_{max} is the time taken for the field to reach $\mu_0 H_{max}$. The resulting $\mu_0 dH/dt$ ranges from about 10^3 T/s to 10^4 T/s in magnitude, much higher than that available in any commercial magnetometer using a superconducting magnet, which is usually smaller than 1 T/s. To reduce possible eddy current heating effects in the sample in pulsed fields, fine Gd_5Ge_4 powder with grains much smaller than the skin depth was homogeneously mixed with the SiO_2 powder. Sample 1 (henceforth S1) contained 16 wt.% Gd_5Ge_4 (corresponding to 5% in volume) and 84 wt.% SiO_2. Its magnetization was measured in a liquid helium bath. Sample 2 (henceforth S2) consisted of 64 wt.% Gd_5Ge_4 (corresponding to 50% in volume) and 36 wt.% SiO_2. Its magnetization was measured in a helium exchange gas atmosphere.

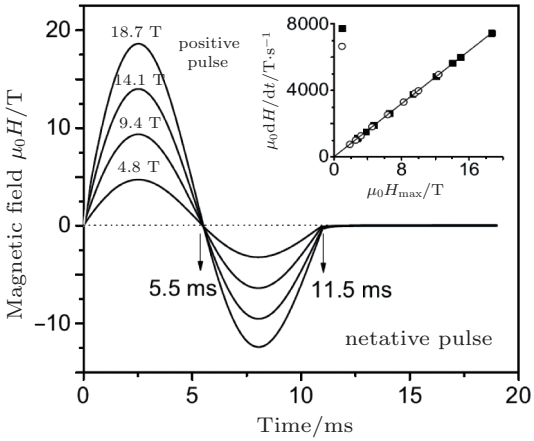


Fig. 47. Time dependent pulsed magnetic fields including both positive and negative pulses. The field sweep rate, $\mu_0 dH/dt$, is defined as $\mu_0 H_{max}/t_{max}$, where t_{max} is the time taken for the field to reach the first peak value $\mu_0 H_{max}$. The inset shows that the $\mu_0 dH/dt$ is proportional to $\mu_0 H_{max}$.[109]

Figure 48 shows that the $M(H)$ curve of S1 measured at 4.2 K is nearly irreversible, which can be seen from the FM-like behavior in the following negative pulse. This is similar to that observed in the conventional isothermal magnetization measurements. This also suggests that S1 is in excellent thermal contact with the surroundings (SiO_2 and liquid helium). Figure 49 shows the typical $M(H)$ curves of S2 measured at different temperatures ranging from 4.2 K to 40 K. At 4.2 K, the field-induced AFM–FM transition is now partially reversible, manifested as a magnetization step in the negative pulse. Recalling that S2 contains less SiO_2 powder than S1 and that the measurement is performed in a helium exchange gas rather than by immersion in a liquid helium bath, the heat exchange of S2 with the environment should be much smaller than that of S1. Thus, the pulsed-field magnetization shows that the low-temperature irreversibility of the AFM–FM transition can be destroyed by the MCE, depending on the heat exchange between the sample and its surroundings. The details of magnetization and demagnetization processes as well as their dynamic responses can be found in Ref. [109].

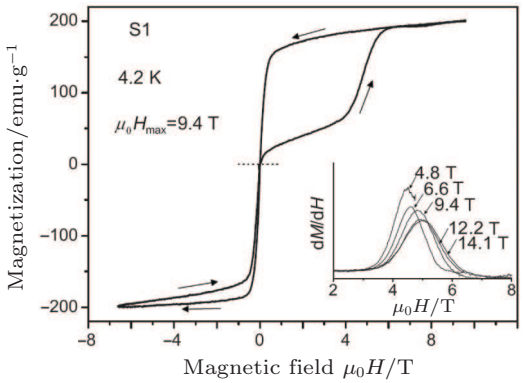


Fig. 48. The $M(H)$ curve of S1 (16 wt.% $Gd_5Ge_4 + 84$ wt.% SiO_2) measured under $\mu_0 H_{max} = 9.4$ T pulsed field at 4.2 K with the sample directly immersed into a liquid helium bath. The arrows show the direction of the variation of the magnetic field. The inset shows the value of dM/dH as a function of H measured at 4.2 K at various field sweep rates.[109]

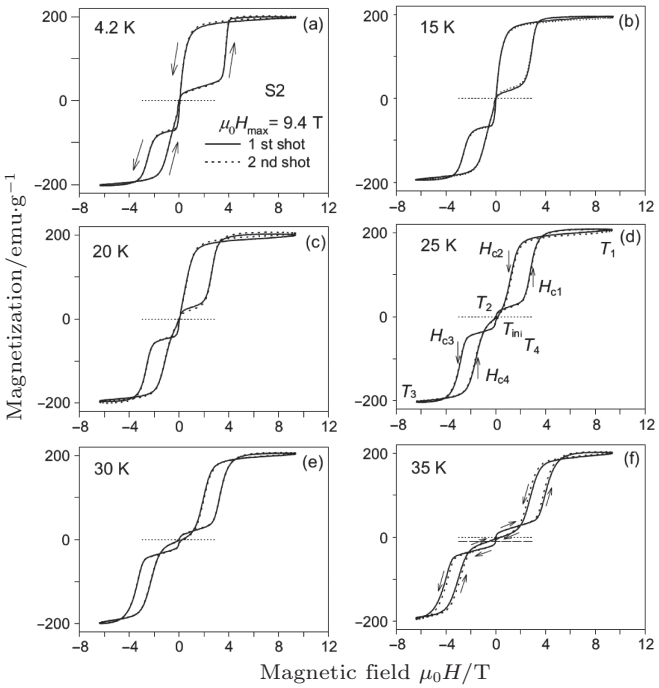


Fig. 49. The $M(H)$ curves of S2 (64 wt.% $Gd_5Ge_4 + 36$ wt.% SiO_2) measured under $\mu_0 H_{max} = 9.4$ T pulsed field at different temperatures ((a) 4.2 K, (b) 15 K, (c) 20 K, (d) 25 K, (e) 30 K, (f) 35 K) with the sample kept in a helium-gas atmosphere. In each measurement, the $M(H)$ curves are recorded twice. The arrows in panels (a) and (f) show the direction of the variation of the magnetic field. The arrows in panel (d) show the positions of the critical fields. The temperatures of the sample in different stages during the pulse are schematically denoted as T_{ini}, T_1, T_2, T_3, and T_4. The horizontal dashed line in panel (f) shows how the zero-field magnetization in the demagnetization curve shifts to a negative value.[109]

3.2.6. Electronic spin resonance across the AFM–FM transition

Unlike the macroscopic magnetization measurements, electron spin resonance (ESR) is a powerful tool to probe the magnetic interactions and correlations in a coupled spin system. The PM resonance in $Gd_5(Si_xGe_{1-x})_4$ was reported at low fields and at a fixed frequency of 9.3 GHz.[110,111] The ESR investigation of polycrystalline Gd_5Ge_4 in high fields and at high frequencies was reported in Ref. [112].

Figures 50 shows the ESR spectra of Gd_5Ge_4 collected at 190 GHz in the zfc H-increasing process. The small anomaly observed in low fields is due to the field-induced AFM–FM transition. A very strong peak is observed at higher fields. At low temperatures, the characteristic field of the peak is well above the critical field for the AFM–FM transition; thus the peak can be ascribed to an FM resonance. With increasing temperature, the FM resonance field H_r remains nearly constant below 20 K but exhibits a significant shift toward a higher field above 20 K. Figure 51 shows the ESR spectra measured at 54.6 GHz, at which the H_r is expected to be lower than the critical field of the AFM–FM transition in the investigated temperature range. Two distinct ESR peaks with a separation of $\Delta H_r = 0.5$ T are observed in the AFM state. Both the ESR peaks do not exhibit any detectable shift with increasing temperature. Since our zfc sample is composed of nearly pure AFM phase with negligible residual FM component (see Figs. 31 and 32), we infer that the two distinct ESR peaks in the AFM state do not originate from the phase separation but from the AFM resonance of the distinct AFM spin system of Gd_5Ge_4, in which the FM-ordered Gd moments in one slab are coupled by an AFM exchange to the FM ordered Gd moments of the neighboring slab.

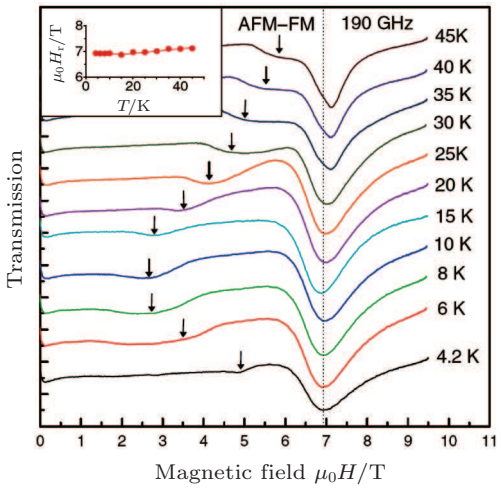


Fig. 50. Temperature dependencies of ESR spectra of Gd_5Ge_4 measured at 190 GHz in the H-increasing process. The down arrows show the AFM–FM transitions. The inset is the resonance field as a function of temperature.[112]

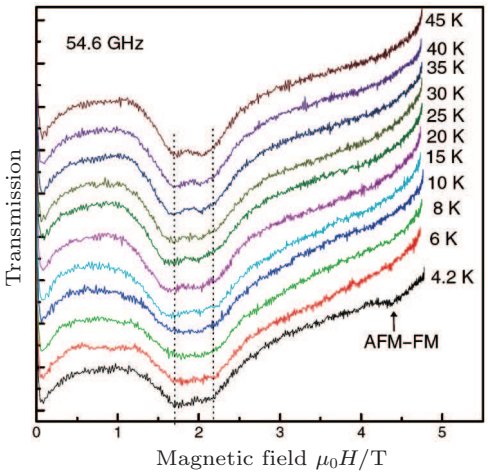


Fig. 51. Temperature dependencies of ESR spectra of Gd_5Ge_4 measured at 54.6 GHz in the H-increasing process. The arrow shows the AFM–FM transition at 4.2 K. The dotted lines show the fields for the AFM resonances.[112]

The frequency-field dependence of ESR at 4.2 K is shown in Fig. 52. In the FM state, the resonance field H_r is proportional to the frequency. A linear least-square fitting gives $g = 1.93$ assuming that all the spins in the FM state maintain perfect parallel alignment during precession. Thus, the g value obtained is much closer to that for noninteracting Gd^{3+} ion ($g = 1.992$), which is surprising because, strictly speaking, it is rather difficult to derive the exact g value due to the

demagnetization factor and the magnetic anisotropy in an ordered phase. However, since our sample is fine powder, these effects might be partially removed. The extrapolation of the H_r–ω curve to zero frequency gives a very small field, showing that the anisotropic energy is indeed small. Hence, the g value derived should be a good approximation. The AFM resonance in the AFM state can be understood within Kittel's formula[113] for a uniaxial antiferromagnet with the magnetic field along the easy axis.

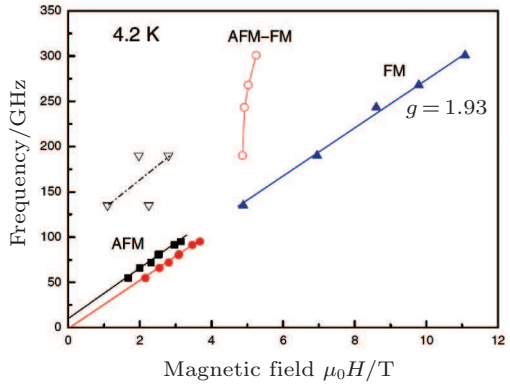


Fig. 52. Frequency-resonance field plot at 4.2 K for Gd_5Ge_4. The fields for the AFM–FM transition are also plotted. The solid lines are the linear fits.[112]

3.2.7. Effects of impurities on the magnetization process

The purity of Gd metal is known to have an essential influence on the magnetostructural transition and the resultant MCE. Like $Gd_5(Si_xGe_{1-x})_4$, the influence of impurities in starting Gd ingots on the field-induced AFM–FM transition in Gd_5Ge_4 is also noted in several reports, the details of which depend on the synthesis conditions in different groups.[90–92,94,95] The complicated influences of impurities upon the magnetization process of Gd_5Ge_4 are reported in Ref. [114]. The polycrystalline sample of Gd_5Ge_4 was prepared by arc melting stoichiometric mixtures of commercial Gd 99.9 wt.% and pure Ge 99.99 wt.% in argon atmosphere. The main impurities in Gd purchased from Baotou, China are C, O, and Ca, but no detailed report of the impurities is available. The XRD patterns in Fig. 53 show that a large amount of the samples crystallize in the orthorhombic structure (*Pnma*), but careful scrutiny reveals the existence of at least $\sim 10\%$ of impurity phases like Gd_5Ge_3 and GdGe, which are marked by asterisks in the figure. The details of the effects of the impurities on the magnetization process are summarized as follows.

First, a residual FM state due to the impurities and an unusually broadened field-induced AFM–FM transition are observed at low temperatures. Unlike the classical AFM–PM transition, the $M(T)$ curves around T_N exhibit a FM–PM-like transition (Fig. 54), signaling the existence of an FM component below T_N. A step-like FM behavior is present on the first H-increasing $M(H)$ curves in the low field range (Fig. 55), further evidencing the existence of a residual FM component in the zfc sample. At 2 K, the AFM–FM transition in the first zfc H-increasing magnetization is so gradual that the critical field associated with the onset of the transition is hardly recognizable. Increasing the magnetic field further leads to a magnetization of $\sim$135 emu/g (5.20 μ_B/Gd) at 7 T, much smaller than the well-known saturation magnetization of 190 emu/g (7.32 μ_B/Gd).[90,95] This indicates that a magnetic field of 7 T is not sufficient to induce the full AFM–FM transition in the present sample.

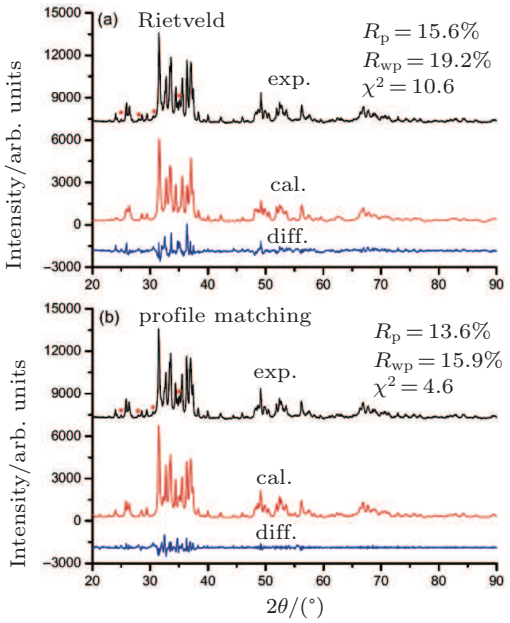


Fig. 53. (a) Rietveld and (b) profile-matching refinements of the XRD data of Gd_5Ge_4 showing the experimental, calculated, and difference patterns. The contributions from secondary phases are marked by asterisks.[114]

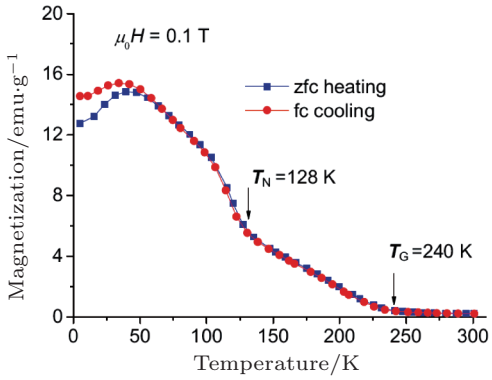


Fig. 54. The $M(T)$ curves of Gd_5Ge_4 measured at 0.1 T.[114]

Second, the dynamic behavior of the unusual magnetization process is observed under pulsed magnetic fields with quite large field-sweep rates (see Fig. 48). As shown in Fig. 56, an enhancement of the low-field FM state is observed in the second pulse performed approximately 10 min after the

completion of the first pulse. This might be a result of combining the MCE,[109] the reduction in flammability[91] and magnetization history of the sample because of the martensitic-like character.[104] Note that as the temperature increases, the dynamic behavior is gradually suppressed, consistent with the observation in steady fields (see Subsection 3.2.3).

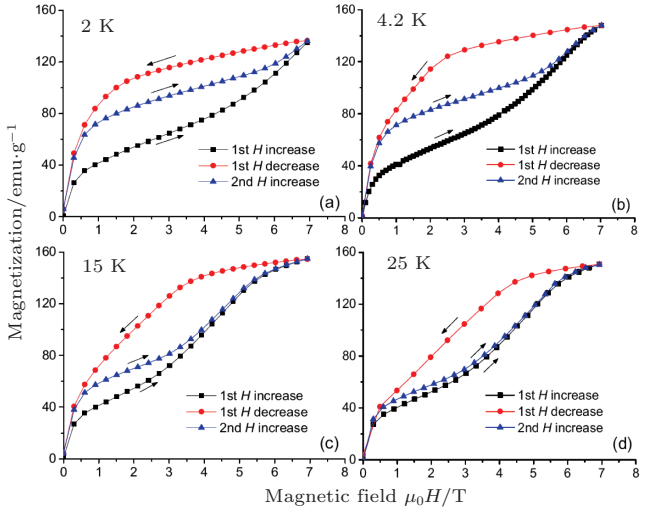


Fig. 55. Isothermal $M(H)$ curves of Gd_5Ge_4 measured at (a) 2 K, (b) 4.2 K, (c) 15 K, and (d) 25 K.[114]

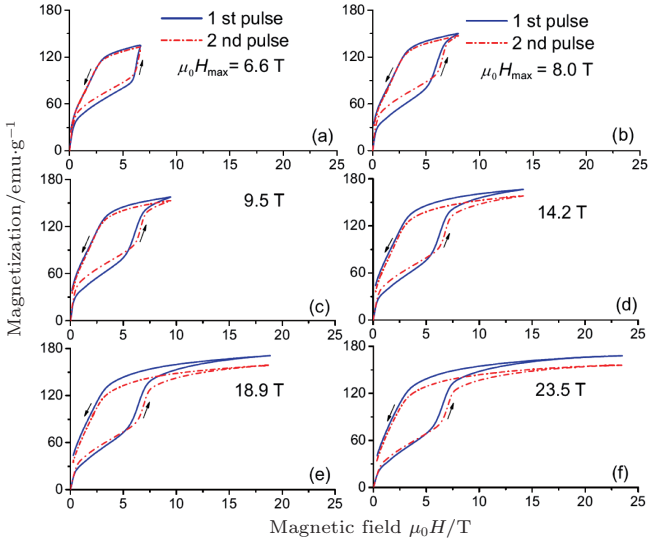


Fig. 56. Nonisothermal $M(H)$ curves of Gd_5Ge_4 measured at 4.2 K using different pulsed magnetic fields ((a) 6.6 T, (b) 8.0 T, (c) 9.5 T, (d) 14.2 T, (e) 18.9 T, (f) 23.5 T).[114]

3.2.8. High magnetic field-induced phase transition and refined magnetic phase diagram

High magnetic field magnetization measurements were performed on Gd_5Ge_4.[115] To minimize the influence of the impurities in Gd ingots upon the magnetostructural transition, polycrystalline Gd_5Ge_4 with little or no FM components[109] was used. Figure 57 shows the $M(H)$ curves of Gd_5Ge_4 measured at 65–130 K under a pulsed magnetic field up to 40 T. With the increase of the magnetic field, all $M(H)$ curves below $T_N = 128$ K exhibit a linear increase at low fields due to the AFM character. Importantly, the results reveal a previously undetected transition between 85 K and 105 K, that is, a distinct second-order AFM–PM transition, followed by a first-order PM–FM transition. The distinct variation of the slope of the $M(H)$ curves is observed around the AFM–PM transition, and its origin could be associated with the MCE and short-range FM correlations. Combining our high-field data and those reported earlier, a new magnetic field-temperature (H–T) phase diagram, in which the AFM, PM, and FM states are well separated, is constructed and depicted in Fig. 58.

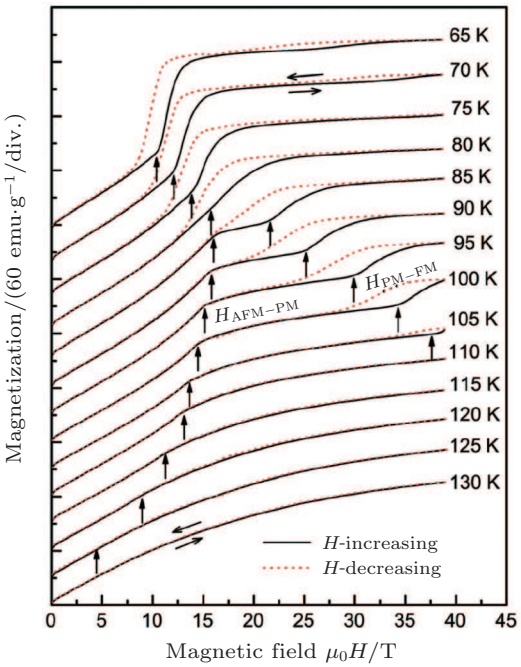


Fig. 57. The $M(H)$ curves of Gd_5Ge_4 measured at 65–130 K. The thin arrows show the direction of the variation of the magnetic field. The thick arrows show the positions of the critical fields.[115]

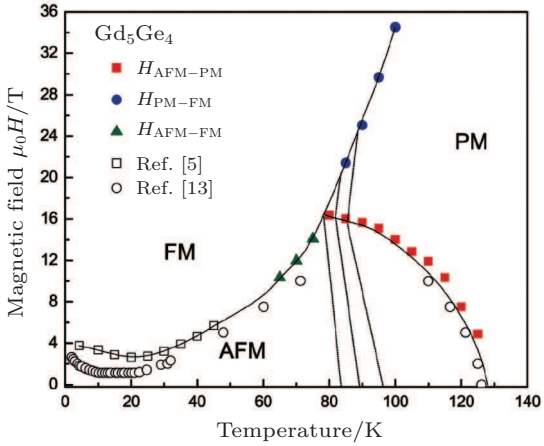


Fig. 58. The H–T phase diagram of Gd_5Ge_4. The inclined dot lines show schematically the magnetization process due to MCE.[115]

4. Summary and remarks

For more than a decade, the discovery of giant MCE in $Gd_5Si_2Ge_2$ has brought about intensive research on the intermetallic compounds R_5M_4 (R = rare earths; M = carbon group elements) and other intermetallic compounds exhibiting first-order magnetic phase transitions. In this article, we have presented the results of our recent investigations of R_5M_4 compounds, including the crystal structures of $Nd_5Si_{4-x}Ge_x$, $Pr_5Si_{4-x}Ge_x$, $Gd_{5-x}La_xGe_4$, La_5Si_4, and Gd_5Sn_4, structural phase transitions and phase relationships of $Nd_5(Si_{1-x}Ge_x)_4$, $Pr_5(Si_{1-x}Ge_x)_4$, and $Gd_5(Si_{1-x}Ge_x)_4$, magnetic structures and magnetic phase transitions of $Pr_5Si_2Ge_2$ and Pr_5Ge_4, and unusual magnetic properties of $Gd_5(Si_{1-x}Ge_x)_4$.

The intermetallic compound R_5M_4 (M = Si, Ge, or a mixture of Si and Ge) crystallizes in one of the three structures, i.e., the tetragonal Zr_5Si_4-type structure (space group $P4_12_12$), the orthorhombic Sm_5Ge_4-type structure (space group $Pnma$), and the monoclinic $Gd_5Si_2Ge_2$-type structure (space group $P112_1/a$), depending on the nature of R and M, the Si/Ge ratio, and temperature. The Sm_5Ge_4 and the $Gd_5Si_2Ge_2$ structures can be viewed as layered structures consisting of slabs stacking along the b direction. The intraslab interaction is strong and FM, while the interslab interaction, FM or AFM, is weak. When the interslab interaction is FM, the M atoms between the slabs are forced to bond covalently, leading to a martensitic-like structural transition from the orthorhombic Gd_5Ge_4-type structure or the monoclinic $Gd_5Si_2Ge_2$-type structure to the orthorhombic Gd_5Si_4-type structure (also with space group $Pnma$).

All the four structure types (Zr_5Si_4, Gd_5Ge_4, $Gd_5Si_2Ge_2$, and Gd_5Si_4 types) have the same basic building unit $[RM_6]R_8$ (M = Si, Ge, or a mixture of Si and Ge) and similar coordination polyhedrons for R atom.[81] The essential difference among these four structure types is the manner of connection between the basic building units, which is responsible for the martensitic-like structural transition and polymorphism of the R_5M_4 compounds as well as the temperature dependent phase relationships. In addition, the distance between magnetic rare earth atoms shows a broad distribution range in R_5M_4 compounds, thus FM and AFM couplings between R atoms can coexist, giving rise to complicated magnetic structures, separate long-range magnetic ordering of R atoms at different crystallographic sites, FM clustering above T_C, complicated dynamics of magnetic properties, etc.

It is well established that the magnetostructural transformation is the origin of the giant MCE of R_5M_4 compounds. Doubtless, new and better magnetic refrigerant materials exhibiting first-order magnetostructural transitions will be discovered in succession. For the practical applications of these materials, the hysteresis of the first-order transition should be diminished. Intensive studies on the magnetostructural transitions are very important not only for applications of these MCE materials, but also for fundamental physics.

References

[1] Pecharsky V K and Gschneidner K A Jr 1999 *J. Magn. Magn. Mater.* **200** 44
[2] Gschneidner K A, Pecharsky V K and Tsokol A O 2005 *Rev. Prog. Phys.* **68** 1479
[3] Pecharsky V K and Gschneidner K A Jr 2006 *Intern. J. Refriger.* **29** 1239
[4] Pecharsky V K, Gschneidner K A Jr, Mudryk Ya and Paudyal D 2009 *J. Magn. Magn. Mater.* **321** 3541
[5] Gschneidner K A Jr 2009 *Acta Mater.* **57** 18
[6] Pecharsky V K and Gschneidner K A Jr 1997 *Phys. Rev. Lett.* **78** 4494
[7] Pecharsky V K and Gschneidner K A Jr 1997 *Appl. Phys. Lett.* **70** 3299
[8] Dan'kov S Yu, Tishin A M, Pecharsky V K and Gschneidner K A Jr 1997 *Rev. Sci. Instr.* **68** 1818
[9] Dan'kov S Yu, Tishin A M, Pecharsky V K and Gschneidner K A Jr 1998 *Phys. Rev. B* **57** 3478
[10] Wang D H, Tang S L, Liu H D, Gao W L and Du Y W 2002 *Intermetallics* **10** 819
[11] Foldeaki M, Giguere A, Chahine R and Bose T K 1998 *Adv. Cryog. Eng.* **43** 1533
[12] de Oliveira N A, von Ranke P J and Troper A 2004 *Phy. Rev. B* **69** 064421
[13] von Ranke P J, Grangeia D F, Caldas A and de Oliveira N A 2003 *J. Appl. Phys.* **93** 4055
[14] Wada H and Tanabe Y 2001 *Appl. Phys. Lett.* **79** 3302
[15] Wada H, Taniguchi K and Tanabe Y 2002 *Mater. Trans.* **43** 73
[16] Morikawa T and Wada H 2004 *J. Magn. Magn. Mater.* **272–276** e583
[17] Tegus O, Br k E, Buschow K H J and de Boer F R 2002 *Nature* **415** 150
[18] Li X W, Tegus O, Zhang L, Dagula W, Br k E, Buschow K H J and de Boer F R 2003 *IEEE Trans. Magn.* **39** 3148
[19] Tegus O, Brück E, Li X W, Zhang L, Dagula W, de Boer F R and Buschow K H J 2004 *J. Magn. Magn. Mater.* **272–276** 2389
[20] Fujita A, Akamatsu K and Fukamichi K 1999 *J. Appl. Phys.* **85** 4756
[21] Hu F X, Shen B G, Sun J R, Cheng Z H, Rao G H and Zhang X X 2001 *Appl. Phys. Lett.* **78** 3675
[22] Wen G H, Zheng R K, Zhang X X, Wang W H, Chen J L and Wu G H 2002 *J. Appl. Phys.* **91** 8537
[23] Chen W, Zhong W, Hou D L, Gao R W, Feng W C, Zhu M G and Du Y W 2002 *J. Phys.: Condens. Matter* **14** 11889
[24] Phan M H, Yu S C and Hur N H 2003 *J. Magn. Magn. Mater.* **262** 407
[25] Xu Y, Menmert U and Hartmann U 2002 *J. Magn. Magn. Mater.* **242–245** 698
[26] Merellon L, Algarabel P A, Ibarra M R, Blasco J, García-Landa B, Arnold Z and Albertini F 1998 *Phys. Rev. B* **58** R14721
[27] Levin E M 2009 *Phys. Rev. B* **80** 144401
[28] Sharath Chandra L S, Pandya S, Vishwakarma P N, Jain D and Ganesan V 2009 *Phys. Rev. B* **79** 052402
[29] Pecharsky V K and Gschneidner K A Jr 1997 *J. Alloys Compd.* **260** 98
[30] Pecharsky A O, Gschneidner K A Jr, Pecharsky V K and Schindler C E 2002 *J. Alloys. Compd.* **338** 126
[31] Ouyang Z W 2010 *J. Appl. Phys.* **108** 033907
[32] Ouyang Z W, Pecharsky V K, Gschneidner K A, Schlagel D L and Lograsso T A 2006 *Phys. Rev. B* **74** 094404
[33] Morellon L, Stankiewicz J, Garcia-Landa B, Algarabel P A and Ibarra M R 1998 *Appl. Phys. Lett.* **73** 3462
[34] Levin E M, Pecharsky V K and Gschneidner K A Jr 1999 *Phys. Rev. B* **60** 7993
[35] Levin E M, Pecharsky V K, Gschneidner K A Jr and Tomlinson P 2000 *J. Magn. Magn. Mater.* **210** 181
[36] Choe W, Pecharsky V K, Pecharsky A O, Gschneidner K A Jr, Young V G Jr and Miller G J 2000 *Phys. Rev. Lett.* **84** 4617
[37] Merellon L, Blasco J, Algarabel P A and Ibarra M R 2000 *Phys. Rev. B* **62** 1022
[38] Pecharsky V K and Gschneidner K A Jr 2001 *Adv. Mater.* **13** 683
[39] Levin E M, Pecharsky V K and Gschneidner K A Jr 2001 *Phys. Rev. B* **63** 174110
[40] Zou M, Tang H, Schlagel D L, Lograsso T A, Gschneidner K A Jr and Pecharsky V K 2006 *J. Appl. Phys.* **99** 08B304

[41] Manekar M, Chattopadhyay M K, Kaul R, Pecharsky V K and Gschneidner K A Jr 2006 *J. Phys.: Condens. Matter* **18** 6017
[42] Casanova F, Labarta A, Batlle X, Vives E, Marcos J, Manosa L and Planes A 2004 *Eur. Phys. B* **40** 427
[43] Casanova F, Labarta A, Batlle X, P ez-Reche F J, Vives E, Manosa L and Planes A 2005 *Appl. Phys. Lett.* **86** 262504
[44] P ez-Reche F J, Casanova F, Vives E, Manosa L, Planes A, Marcos J, Batlle X and Labarta A 2006 *Phys. Rev. B* **73** 014110
[45] Roy S B, Chattopadhyay M K, Chaddah P, Moore J D, Perkins G K, Cohen L F, Gschneidner K A Jr and Pecharsky V K 2006 *Phys. Rev. B* **74** 012403
[46] Roy S B, Chattopadhyay M K, Banerjee A, Chaddah P, Moore J D, Perkins G K, Cohen L F, Gschneidner K A Jr and Pecharsky V K 2007 *Phys. Rev. B* **75** 184410
[47] Morellon L, Magen C, Algarabel P A, Lbarra M R and Ritter C 2001 *Appl. Phys. Lett.* **79** 1318
[48] Tegus O, Dagula O, Brück, Zhang L, de Boer F R and Buschow K H J 2002 *J. Appl. Phys.* **91** 8534
[49] Ritter C, Morellon L, Algarabel P A, Magen C and Ibarra M R 2002 *Phys. Rev. B* **65** 094405
[50] Magen C, Algarabel P A, Morellon L, Ara o J P, Ritter C, Ibarra M R, Pereira A M and Sousa J B 2006 *Phys. Rev. Lett.* **96** 167201
[51] Zou M, Pecharsky V K, Gschneidner K A Jr, Schlagel D L and Lograsso T A 2008 *Phys. Rev. B* **78** 014435
[52] Tian W, Kreyssig A, Zarestky J L, Tan L, Nandi S, Goldman A I, Lograsso T A, Schlagel D L, Gschneidner K A Jr, Pecharsky V K and McQueeney R J 2009 *Phys. Rev. B* **80** 134422
[53] Morellon L, Ritter C, Magen C, Algarabel P A and Ibarra M R 2003 *Phys Rev. B* **68** 024417
[54] Garlea V O, Zarestky J L, Jones C Y, Lin L L, Schlagel D L, Lograsso T A, Tsokol A O, Pecharsky V K, Gschneidner K A Jr and Stassis C 2005 *Phys. Rev. B* **72** 104431
[55] Zou M, Mudryk Ya, Pecharsky V K, Gschneidner K A Jr, Schlagel D L and Lograsso T A 2007 *Phys. Rev. B* **75** 024418
[56] Morellon L, Arnold Z, Magen C, Ritter C, Prokhnenko O, Skorokhod Y, Algarabel P A, Ibarra M R and Kamarad J 2004 *Phys. Rev. Lett.* **93** 137201
[57] Pecharsky V K, Pecharsky A O, Mozharivskyj Y, Gschneidner K A Jr and Miller G J 2003 *Phys. Rev. Lett.* **91** 207205
[58] Mozharivskyj Y, Pecharsky A O, Pecharsky V K, Miller G J and Gschneidner K A Jr 2004 *Phys. Rev. B* **69** 144102
[59] Pecharsky A O, Gschneidner K A Jr, Pecharsky V K, Schlagel D L and Lograsso T A 2004 *Phys. Rev. B* **70** 144419
[60] Mudryk Ya, Singh N K, Pecharsky V K, Schlagel D L, Lograsso T A and Gschneidner K A Jr 2012 *Phys. Rev. B* **85** 094432
[61] Magen C, Ritter C, Morellon L, Algarabel P A, Ibarra M R, Tsokol A O, Gschneidner K A Jr and Pecharsky V K 2006 *Phys. Rev. B* **74** 174413
[62] Magen C, Morellon L, Arnold Z, Algarabel P A, Ritter C, Ibarra M R, Kamarad J, Tsokol A O, Gschneidner K A Jr and Pecharsky V K 2006 *Phys. Rev. B* **74** 134427
[63] Marcano N, Algarabel P A, Rodriguez Fernandez J, Magen C, Morellon L, Singh N K, Schlagel D L, Gschneidner K A Jr, Pecharsky V K and Ibarra M R 2012 *Phys. Rev. B* **85** 024408
[64] Smith G S, Tharp A G and Johnson Q 1966 *Nature* **210** 1148
[65] Smith G S, Johnson Q and Tharp A G 1967 *Acta Crystallogr.* **22** 269
[66] Smith G S, Tharp A G and Johnson Q 1967 *Acta Crystallogr.* **22** 940
[67] Holtzberg F, Gambino R J and Mequire R T 1967 *J. Phys. Chem. Solids* **28** 2283
[68] Yang H F, Rao G H, Chu W G, Liu G Y, Ouyang Z W and Liang J K 2002 *J. Alloys Compd.* **334** 131
[69] Yang H F, Rao G H, Liu G Y, Ouyang Z W, Liu W F, Feng X M, Chu W G and Liang J K 2002 *J. Alloys Compd.* **346** 190
[70] Yang H F, Rao G H, Liu G Y, Ouyang Z W, Liu W F, Feng X M, Chu W G and Liang J K 2003 *J. Alloys Compd.* **348** 150
[71] Yang H F, Rao G H, Liu G Y, Ouyang Z W, Liu W F, Feng X M, Chu W G and Liang J K 2003 *Physica B* **325** 293
[72] Callaway J 1991 *Quantum Theory of the Solid State* (2nd edn.) (New York: Academic Press) p. 860
[73] Bleaney B I and Bleaney B 1965 *Electricity and Magnetism* (Oxford: Clarendon Press) p. 621
[74] Miller G L 1996 *Chemistry, Structure and Bonding of Zintl Phases and Ions* (New York: VCH Publishers) pp. 1–59
[75] Yang H F, Rao G H, Chu W G, Liu G Y, Ouyang Z W and Liang J K 2002 *J. Alloys Compd.* **339** 189
[76] Yang H F, Rao G H, Liu G Y, Ouyang Z W, Liu W F, Feng X M, Chu W G and Liang J K 2003 *J. Magn. Magn. Mater.* **263** 146
[77] Gschneidner K A Jr, Pecharsky V K, Pecharsky A O, Ivtchenko V V and Levin E M 2000 *J. Alloys Compd.* **303–304** 214
[78] Kirchmayr H R and Poldy C A 1979 *Handbook on the Physics and Chemistry of Rare Earth* (Gschneidner K A Jr and Eyring L, ed.) Vol. 2 (The Netherlands: North-Holland) p. 64
[79] Yang H F, Rao G H, Liu G Y, Ouyang Z W, Feng X M, Liu W F, Chu W G and Liang J K 2003 *Phys. Stat. Sol. (a)* **198** 156
[80] Yang H F, Rao G H, Liu G Y, Ouyang Z W, Feng X M, Liu W F, Chu W G and Liang J K 2002 *J. Phys.: Condens. Matter* **14** 9705
[81] Wang Y C, Yang H F, Huang Q, Duan L B, Lynn J W and Rao G H 2007 *Phys. Rev. B* **76** 064425
[82] Rao G H, Huang Q, Yang H F, Ho D L, Lynn J W and Liang J K 2004 *Phys. Rev. B* **69** 094430
[83] Yang H F, Rao G H, Liu G Y, Ouyang Z W, Liu W F, Feng X M, Chu W G and Liang J K 2003 *J. Alloys Compd.* **361** 113
[84] Yang H F, Rao G H, Liu G Y, Ouyang Z W, Liu W F, Feng X M, Chu W G and Liang J K 2004 *J. Alloys Compd.* **368** 248
[85] Ryan D H, Elouneg-Jamr M, Van Lierop J, Altounian Z and Wang H B 2003 *Phys. Rev. Lett.* **90** 117202
[86] Wang H B, Altounian Z and Ryan D H 2002 *Phys. Rev. B* **66** 214413
[87] Liu Q L, Rao G H, Yang H F and Liang J K 2001 *J. Alloys Compd.* **325** 50
[88] Rao G H 2000 *J. Phys: Condens. Matter* **12** L93
[89] Casanova F, Labarta A and Batlle X 2005 *Phys. Rev. B* **72** 172402
[90] Hardy V, Majumdar S, Crowe S J, Lees M R, McK Paul D, Hervé L, Maignan A, Hébert S, Martin C, Yaicle C, Hervieu M and Raveau B 2004 *Phys. Rev. B* **69** R020407
[91] Velez S, Hernandz J M, Fernandz A, Maci F, Magen C, Algarabel P A, Tejada J and Chudnovsky E M 2010 *Phys. Rev. B* **81** 064437
[92] Levin E M, Gschneidner K A Jr and Pecharsky V K 2002 *Phys. Rev. B* **65** 214427
[93] Tan L, Kreyssig A, Kim J W, Goldman A I, McQueeney R J, Wermeille D, Sieve B, Lograsso T A, Schlagel D L, Budko S L, Pecharsky V K and Gschneidner K A Jr 2005 *Phys. Rev. B* **71** 214408
[94] Magen C, Arnold Z, Morellon L, Skorokhod Y, Algarabel P A, Ibarra M R and Kamarad 2003 *Phys. Rev. Lett.* **91** 207202
[95] Tang H, Pecharsky V K, Gschneidner K A Jr and Pecharsky A O 2004 *Phys. Rev. B* **69** 064410
[96] Ouyang Z W, Pecharsky V K, Gschneidner K A Jr, Schlagel D L and Lograsso T A 2006 *Phys. Rev. B* **74** 024401
[97] Néel L 1936 *Ann. Phys. (Paris)* **5** 232
[98] Lynn J W, Heller P and Lurie N A 1977 *Phys. Rev. B* **16** 5032
[99] Shapira Y and Foner S 1970 *Phys. Rev. B* **1** 3083
[100] Birgeneau R J, Shirane G, Blumet M and Koehler W C 1974 *Phys. Rev. Lett.* **33** 1098
[101] Tsukada I, Takeya J, Masuda T and Uchinokura K 2001 *Phys. Rev. Lett.* **87** 127203
[102] Ouyang Z W, Pecharsky V K, Gschneidner K A Jr, Schlagel D L and Lograsso T A 2007 *Phys. Rev. B* **76** 134415
[103] Levin E M, Gschneidner K A Jr, Lograsso T A, Schlagel D L and Pecharsky V K 2004 *Phys. Rev. B* **69** 144428
[104] Ouyang Z W, Pecharsky V K, Gschneidner K A Jr, Schlagel D L and Lograsso T A 2007 *Phys. Rev. B* **76** 134406
[105] Ugurlu O, Chumbley L S, Schlagel D L and Lograsso T A 2006 *Acta Mater.* **54** 1211
[106] Griffiths R B 1969 *Phys. Rev. Lett.* **23** 17
[107] Salamon M B, Lin P and Chun S H 2002 *Phys. Rev. Lett.* **88** 197203
[108] Castro Neto A H, Castilla G and Jones B A 1998 *Phys. Rev. Lett.* **81** 3531
[109] Ouyang Z W, Nojiri H, Yoshii S, Rao G H, Wang Y C, Pecharsky V K and Gschneidner K A Jr 2008 *Phys. Rev. B* **77** 184426
[110] Pires M J M, Carvalho A M G, Gama S, da Silva E C, Coelho A A and Mansanares A M 2005 *Phys. Rev. B* **72** 224435
[111] Pires M J M, Mansanares A M, da Silva E C, Carvalho A M G, Gama S and Coelho A A 2006 *Phys. Rev. B* **73** 144404
[112] Ouyang Z W, Nojiri H, Yoshii S, Rao G H and Wang Y C 2009 *Phys. Rev. B* **80** 054401
[113] Keffer F and Kettel C 1952 *Phys. Rev.* **85** 329
[114] Ouyang Z W, Xia Z C, Wang Y C and Rao G H 2011 *J. Appl. Phys.* **109** 023901
[115] Wu Y Y, Xia Z C, Ouyang Z W, Huang Y and Li L 2011 *J. Appl. Phys.* **109** 083911